

Ocean Remote Sensing Using Spaceborne GNSS-Reflectometry: A Review

Jinwei Bu^{ID}, Member, IEEE, Xinyu Liu^{ID}, Qiulan Wang, Linghui Li, Xiaoqing Zuo^{ID}, Kegen Yu^{ID}, Senior Member, IEEE, and Weimin Huang^{ID}, Senior Member, IEEE

Abstract—Spaceborne global navigation satellite system reflectometry (GNSS-R) is an emerging remote sensing technology that utilizes Earth surface reflections of GNSS signals to monitor geo-physical parameters. With its unique advantages of high spatiotemporal resolution, low observational cost, wide coverage, and all-weather operation, GNSS-R has found extensive applications in ocean remote sensing. Recent successful launches of spaceborne GNSS-R platforms, such as TechDemoSat-1 in 2014, Cyclone GNSS in 2016, BuFeng-1 A/B in 2019, and FengYun-3E in 2021, have opened up new opportunities in this field. This article provides a comprehensive overview of the latest advancements in the application of spaceborne GNSS-R in ocean remote sensing. It covers satellite missions related to spaceborne GNSS-R and explores various methods and techniques for ocean remote sensing applications, including sea surface wind mapping, hurricanes, typhoons, and tropical cyclones monitoring, tsunamis and storm surges detection, sea surface altimetry and wave height measurement, sea ice sensing, and rainfall estimation, among others. Furthermore, the article discusses the challenges, prospects, and future outlook of spaceborne GNSS-R.

Index Terms—BuFeng-1 (BF-1) A/B, cyclone global navigation satellite system (CYGNSS), FengYun-3E, geophysical parameters, ocean remote sensing, spaceborne GNSS reflectometry, Tech-DemoSat-1 (TDS-1).

I. INTRODUCTION

CURRENTLY, there are more than 100 operational navigation satellites in space, including the four major global satellite navigation systems: China's BeiDou navigation satellite system (BDS), the European Union's Galileo, Russia's

Manuscript received 17 January 2024; revised 31 March 2024 and 24 May 2024; accepted 20 June 2024. Date of publication 24 June 2024; date of current version 26 July 2024. This work was supported in part by Yunnan Fundamental Research Projects under Grant 202401CF070151, in part by the National Natural Science Foundation of China under Grant 42174022 and Grant 42161067, in part by the major scientific and technological projects of Yunnan province: Research on key technologies of ecological environment monitoring and intelligent management of natural resources in Yunnan under Grant 202202AD080010, and in part by the Innovative Training Plan Program for College Students of Yunnan province under Grant S202310674221. (*Corresponding author: Xinyu Liu.*)

Jinwei Bu, Xinyu Liu, Qiulan Wang, Linghui Li, and Xiaoqing Zuo are with the Faculty of Land Resources Engineering, Kunming University of Science and Technology, Kunming 650093, China (e-mail: b_jinwei@kust.edu.cn; liuxinyu6@stu.kust.edu.cn; 202210108133@stu.kust.edu.cn; lilinghui@stu.kust.edu.cn; zxq@kust.edu.cn).

Kegen Yu is with the School of Environment Science and Spatial Informatics, China University of Mining and Technology, Xuzhou 221116, China (e-mail: kegen.yu@cumt.edu.cn).

Weimin Huang is with the Department of Electrical and Computer Engineering, Memorial University of Newfoundland, St. John's, NL A1B 3X5, Canada (e-mail: weimin@mun.ca).

Digital Object Identifier 10.1109/JSTARS.2024.3418429

GLONASS, and the United States' global positioning system (GPS). In addition, India's Indian Regional Navigation Satellite System and Japan's Quasi-Zenith Satellite System (QZSS) contribute to the global navigation satellite network. These systems offer all-weather capability, near real-time data, high accuracy, and continuous transmission of L-band signals, making them widely used for positioning, navigation, and timing applications [1].

As satellite constellations continue to improve and expand, the applications of global navigation satellite systems (GNSS) systems have become increasingly diverse. In addition to their primary functions in positioning, timing, and navigation, GNSS systems are also utilized for remote sensing by analyzing surface-reflected GNSS signals. This technique, known as GNSS-R remote sensing, is a relatively new and cost-effective method that capitalizes on the processing and analysis of GNSS signals reflected from the Earth's surface to measure various geophysical parameters [2].

GNSS-R can be classified into four types based on the platforms receiving the signals: ground-based GNSS-R, shipborne GNSS-R, airborne GNSS-R, and spaceborne GNSS-R. Each type has its unique advantages and applications. In terms of remote sensing applications, GNSS-R can be categorized into three major domains: atmosphere remote sensing, ocean remote sensing, and land remote sensing [3].

Atmosphere remote sensing using GNSS-R mainly focuses on monitoring the ionosphere, which provides valuable information for weather prediction and atmospheric studies. Ocean remote sensing with GNSS-R enables the retrieval of essential oceanic parameters, such as sea surface wind speed and significant wave height, etc. This information is crucial for understanding ocean dynamics, climate patterns, and maritime transportation. Land remote sensing using GNSS-R encompasses applications such as soil moisture retrieval, vegetation parameters retrieval, soil freeze-thaw states monitoring, snow depth estimation, and surface water detection, etc [4]. These applications contribute to improved agriculture, hydrology, and climate modeling.

In 1988, Hall and Cordey [5] introduced the concept of GNSS bistatic radar, which paved the way for using GNSS reflection signals in remote sensing applications. In 1993, Martin-Neira [6] proposed the use of GNSS reflection signals for ocean altimetry, highlighting the potential of GNSS-R for ocean observation. In 1998, Garrison et al. [7] conducted airborne experiments that validated the correlation between scattered GNSS signals and sea surface roughness under different sea conditions.

Building upon these advancements, Zavorotny and Voronovich developed a two-dimensional delay-Doppler power model for GNSS scattered signals using the bistatic radar equation, the Kirchhoff approximation, and geometric optics in 2000. This model laid the theoretical foundation for retrieving sea surface wind fields from scattered signals [8] as well as other applications.

In 2002, Lowe et al. [9] accomplished the first detection of GNSS reflection signals from a spaceborne platform, demonstrating the feasibility of spaceborne GNSS-R for remote sensing. In 2003, the United Kingdom Disaster Monitoring Constellation (U.K.-DMC) satellite, equipped with a GPS-R receiver, successfully received and processed GPS L1 C/A code reflection signals, confirming its capacity for retrieving sea winds and sea ice from spaceborne platforms [10].

In 2014, Clarizia et al. [11] proposed the minimum variance (MV) estimator for GNSS-R wind speed estimation, achieving an improved accuracy with a root-mean-square error (RMSE) of 1.65 m/s. In the same year, the U.K.'s TechDemoSat-1 (TDS-1) satellite, carrying the Spaceborne GNSS Receiver for Sensing the Earth's Surface (SGR-ReSI), was launched. The SGR-ReSI system coherently processed GPS L1 C/A code direct reflection signals and obtained a significant amount of delay-Doppler map (DDM) data. With the TDS-1 data, Foti et al. [12] successfully retrieved sea surface wind speed with an accuracy of about 2.2 m/s for wind in the range of 3–18 m/s.

In December 2016, NASA developed the Cyclone Global Navigation Satellite System (CYGNSS) which consists of eight small satellites, providing more opportunities for utilizing GNSS-R technology to retrieve sea surface wind speeds [13]. On June 5, 2019, China launched the BuFeng-1 (BF-1) A/B dual satellite mission, i.e., China's first dedicated GNSS-R satellite mission. With the launch of these satellites, China became the fourth country to deploy GNSS-R satellites in Earth orbit, following the U.K., the U.S., and Japan. The BF-1 A/B mission also obtained the world's first spaceborne BDS DDM [14]. In addition, on July 5, 2021, China launched the Feng Yun-3E meteorological satellite, which has been utilizing GNSS-R data for sea surface wind speed retrieval [15]. This satellite mission also focuses on GNSS radio occultation (GNSS-RO) applications. Furthermore, a detailed overview of the GNSS deflection, radio occultation, and scattering measurements on board the International Space Station, proposed by European Space Agency (ESA), is presented in the literature [16]. The experiment is planned for oceanic, atmospheric, and terrestrial remote sensing using GNSS signals of opportunity.

Several papers [1], [2], [3], [4], [17] reviewing the applications of GNSS-R technology in various fields have been published. However, each of these papers tends to focus only on a specific application rather than providing a comprehensive review of all the ocean-related applications for spaceborne GNSS-R. Therefore, there is a need for a comprehensive review paper that encompasses a wide range of applications, including but not limited to sea surface altimetry, sea surface wind speed and direction estimation, and sea ice monitoring. Such a review paper would provide valuable insights into the diverse applications of

spaceborne GNSS-R technology in monitoring and studying the marine environment.

The rest of the article is organized as follows. Section II provides an overview of the key messages of the spaceborne GNSS-R mission. Section III provides an overview of the methods and research status of using spaceborne GNSS-R data to retrieve sea surface wind speed and direction, as well as potential applications in detecting hurricanes, typhoons, and tropical cyclones. Section IV provides an overview of the demonstration of using spaceborne GNSS-R for sea surface height (SSH) and the methods for retrieving sea surface wave height (i.e., significant wave height and swell height), as well as its potential in detecting tsunamis and storm surges. Section V provides an overview of the advanced methods and current status of research on the use of spaceborne GNSS-R for sea ice detection and retrieval of sea ice concentration and thickness. Section VI provides an overview of the current state of research and challenges in spaceborne GNSS-R rainfall detection (RD) and rainfall intensity (RI) retrieval. Section VII outlines other innovative applications of spaceborne GNSS-R technology. Section VIII presents conclusions and future research directions.

II. SPACEBORNE GNSS-R-RELATED SATELLITE MISSIONS

Currently, approximately ten satellite missions have payloads specifically designed for GNSS-R ocean and/or land applications. Table I lists the key information, including the GNSS-R types, frequency bands, polarizations, and associated GNSS systems, about these spaceborne GNSS-R missions. Each mission is summarized as follows.

U.K.-DMC: The U.K.-DMC satellite, launched in December 2003, is the first GNSS-R satellite developed by Surrey Satellite Technology Limited (SSTL). It carries four primary payloads, one of which is specifically dedicated to experimental purposes to showcase the potential applications of GNSS-R technology. While the data collected by the U.K.-DMC satellite have not been extensively utilized in remote sensing research likely due to limited data available, the satellite has successfully sensed ocean roughness [18]. The experiments and data collection conducted by the U.K.-DMC satellite have played a significant role in optimizing the design of SSTL's new GNSS-R device [12].

TDS-1: On July 8, 2014, the U.K. launched the TDS-1 satellite, which carried GNSS-R receivers also developed by SSTL. The TDS-1 satellite was retired in December 2018. In four years, TDS-1 recorded a large amount of spaceborne GNSS-R data, which is widely used in scientific and technological research [19], [20].

CYGNSS: Following TDS-1, on December 15, 2016, NASA launched eight microsatellites to monitor tropical cyclones with the primary goal of improving the accuracy of hurricane intensity measurements and predictions [34], [35]. The project is led by the University of Michigan in the United States. CYGNSS has also generated a large number of data, which are also used to retrieve various ocean and land parameters in addition to its initially targeted ones.

TABLE I
GNSS-R SPACEBORNE MISSIONS

| Missions | Launch country (Area) | Launch date | GNSS-R type | Frequency band/polarization | GNSS system |
|--------------------------------------|-----------------------|-------------------------|--|-----------------------------|----------------------------------|
| UK-DMC [10] | UK | 2003-12 | cGNSS-R | L1/ LHCP | GPS |
| UK-TDS-1 [19] | UK | 2014-07 | cGNSS-R | L1/ LHCP | GPS |
| CYGNSS [21] | America | 2016-12 | cGNSS-R cGNSS-R rGNSS-R iGNSS-R | L1/ LHCP | GPS GPS |
| ³ Cat-2 [22] | Spain | 2016-08 | rGNSS-R iGNSS-R | L1/ LHCP, RHCP | GLONASS Galileo BeiDou |
| SMAP GNSS-R [23] | America | 2015-01 | cGNSS-R | L2/H, V | GPS |
| BuFeng-1 A/B [14] | China | 2019-06 | cGNSS-R | L1/ LHCP | BeiDou GPS |
| Spire [24] | America | 2019-01 | cGNSS-R | L1, L2/ LHCP | Galileo BeiDou |
| FengYun-3E/3G/3F [25], [26], [27] | China | 2021-07/2023-04/2023-08 | cGNSS-R | L1/ LHCP | QZSS GPS Galileo BeiDou |
| ³ Cat-5 A/B (FSSCat) [28] | Spain | 2020-09 | cGNSS-R | L1/ LHCP | GPS Galileo |
| ³ Cat-4 [29], [30] | Spain | Summer 2024 (expected) | cGNSS-R | L1, L2/ LHCP | GPS Galileo |
| PRETTY [31] | ESA | 2022 | iGNSS-R | L1/ LHCP | GPS Galileo |
| TRITON (FORMOSAT-7R) [32] | Taiwan, China | 2022 | cGNSS-R | L1/ LHCP | GPS Galileo QZSS |
| HydroGNSS [33] | ESA | In the future | cGNSS-R | L1, E1/ LHCP, RHCP | GPS Galileo |

³Cat-2: ³Cat-2 is a six-unit cube satellite demonstration mission for Earth observation using GNSS-R [22]. The space-craft carries the main payload of P(Y) and C/A reflectometer (PYCARO), and the ³Cat-2 payload is designed with dual frequency (L1, L2) and dual 96 polarization (LHCP, RHCP) 3×2 patch antenna arrays to perform GNSS-R measurements over oceans, land, and ice using multiple constellation signals (GPS, GLONASS, Galileo, and BDS). ³Cat-2 also aims to provide scientifically valuable data in a very cost-effective manner, which may open the door for future GNSS-R instrument constellations.

SMAP: The soil moisture active passive detection (SMAP) mission, launched in January 2015 and became operational in April 2015, is designed to measure soil moisture levels on regional and global scales. The mission aims to gather global soil moisture data every two to three days. The frequent and reliable measurements obtained by SMAP contribute to improving the prediction capabilities of weather and climate models. The radar receiver of the SMAP mission was tuned to the GPS L2 frequency (1227.6 MHz) to collect GPS signals reflected by the Earth's surface [23]. The SMAP mission utilizes reflected GPS signals to obtain additional information about soil moisture and other geophysical parameters. By utilizing the GPS signals,

SMAP enhances its capabilities to monitor and study soil moisture dynamics, further enhancing our understanding of Earth's water cycle.

BF-1 A/B: On June 5, 2019, China Aerospace Science and Technology Corporation launched the dual satellite "BuFeng-1" from the Yellow Sea. The main focus of this satellite mission is to test the ability of GNSS-R to monitor sea surface wind fields, especially typhoons [14].

Spire: The Spire constellation conducts various GNSS Earth observation missions, including radio occultation (GNSS-RO), ionized layers, and space weather measurements, as well as precise orbit determination [36], [37]. In December 2019, Spire launched two new satellites to perform GNSS reflection measurements. Compared to CYGNSS, Spire's GNSS-R satellite has been specifically optimized for land applications with hardware and software improvements for better signal calibration and increased data acquisition per satellite. With more Spire satellites entering orbit, the potential for more powerful GNSS-R soil moisture retrieval with finer spatial resolution in the near future is promising. Current and future GNSS-R satellites from Spire will provide unprecedented next-day global coverage at subkilometer spatial resolution, making this intensive data collection crucial for various land and marine applications.

FengYun-3E/3G /3F: On July 5, 2021, China's FengYun-3E meteorological satellite was launched, carrying GNOS II GNSS remote sensing instruments and 11 payloads, including integrated GNSS-RO and GNSS-R payload for sensing ionospheric, atmospheric, and oceanic parameters for the first time [38]. FengYun-3G is China's first low-inclination orbit precipitation measurement satellite, which was successfully launched on April 16, 2023. The GNOS-II instrument (Global Navigation Satellite Occultation Sounder-II) is one of the payloads of China's low-orbit meteorological satellite system, FengYun-3 (FY-3) series, and its main mission is to carry out the detection of GNOS occultation signals and reflectance signals, and to provide the parameters of atmosphere and ionosphere, atmospheric temperature profile and wet atmospheric profile, sea surface wind speed, soil moisture, and to provide high-quality datasets for numerical weather prediction, climate change, and space weather. The FengYun-3F satellite was launched on August 3, 2023, which is a continuation of the GNSS GNOS-II on the FY-3E satellite, and the GNOS-II on the FY-3F satellite is one of the 3 batch of payloads, and its main mission is to carry out the GNSS occultation detection and the ocean reflection detection to provide the atmospheric and ionospheric parameter profiles, sea surface wind speed, and to provide high-quality datasets for numerical weather prediction, climate change, and space weather. It provides high-quality datasets for numerical weather prediction, climate change, and space weather.

³Cat-5 A/B (FSSCat): FSSCat is an innovative mission consisting of two joint six-unit cube satellites (³Cat-5/A and ³Cat-5/B) [28]. FSSCat was the first mission contributing to the Copernican System (Land and Marine Environmental Services), which was successfully launched on September 3, 2020, providing L-band GNSS-R measurements. It carries dual microwave payloads (GNSS reflectometer and L-band radiometer with interference detection/mitigation function) and multibeam spectrum optical payloads to measure soil moisture, ice cover range and thickness, and detect melting pools on ice. It also includes a technical demonstrator for optical intersatellite link and concept validation for a federated satellite system.

³Cat-4: ³Cat-4 is the fourth member of the CubeSat series from the nanosatellite laboratory at the University of Polytechnic de Catalunya. This task aims to demonstrate the capabilities of nanosatellites, especially those based on the unit cube satellite standard, using GNSS-R and L-band microwave radiation measurements for Earth observation and automatic recognition services [29].

PRETTY: One of the purposes of the reflectometer payload on passive reflectometry and dosimetry (PRETTY) is to demonstrate the technical feasibility of phase height measurement (or phase-delay height measurement), as done in [39] and [40], at grazing incidence angles. PRETTY flies in low Earth orbit (LEO) and measures reflected and direct GNSS signals for altitude and scattering measurements at very high incidence angles based on interferometry techniques. The signal processing core of PRETTY is an on-chip system, consisting of a dual-core ARM processor and an on-chip field programmable gate array structure [31].

TRITON (FORMOSAT-7R): The FORMOSAT-7R (FS-7R) program is a GNSS reflection measurement task for remote sensing of ocean surface roughness and wind speed, attempting to provide key data for severe weather research and prediction. Compared with the GNSS-R receivers in TDS-1 and CYGNSS, the GNSS-R payload has some distinct characteristics. The GNSS-R payload is a powerful GNSS receiver because it can handle scattered GPS, Galileo, and QZSS signals [32], [41].

HydroGNSS: With funding from the ESA Scout program, SSTL is building hydrology using global navigation satellite system reflections (HydroGNSS), a 55-kg small satellite used to measure climate change variables [33]. HydroGNSS employs GNSS-R technology, using existing signals from global navigation satellites such as GPS and Galileo as radar sources, to measure key hydroclimate variables, including soil moisture, freeze/thaw surface state, floods and wetlands, and above-ground biomass. HydroGNSS provides a new capability for monitoring highly dynamic phenomena and helps fill the gaps in monitoring Earth's vital signs in the future. The HydroGNSS mission aims to assist in climate change mitigation by leveraging space technology to provide valuable measurements.

In addition to the aforementioned GNSS-R missions, there are other spaceborne missions aimed at utilizing reflected GNSS signals and other opportunistic signals for various geophysical applications. For example, on July 5, 2019, the DOT-1 satellite, which is the third satellite designed by SSTL for GNSS-R research, was launched. The payload carried on the DOT-1 satellite is intended to test advanced electronic equipment such as antenna technology, which can be utilized for future spaceborne technologies [42]. On July 3, 2021, the first commercial satellite with a GNSS-R payload, Jilin-01B, was launched into space. The GNSS-R payload is carried onboard the Jilin-01B satellite developed by Changguang Satellite Technology, Co., Ltd., and it is utilized for detecting a range of oceanic parameters [43].

III. RETRIEVAL OF SEA SURFACE WIND SPEED AND DIRECTION

A. Sea Surface Wind Speed Retrieval

Currently, there are four types of methods for retrieving ocean surface wind speed using spaceborne GNSS-R: waveform matching, empirical modeling, intelligent optimization algorithms, and machine/deep learning. Among these, machine learning approaches have shown the highest accuracy in wind speed estimation. The waveform matching method involves comparing the observed GNSS reflection signal to a preconstructed simulated waveform to retrieve wind speed. This method has been proven to provide high accuracy. For example, Li and Huang [44] used the least squares (LS) method to fit the two-dimensional simulated GNSSR DDM to measured data and achieved a wind speed error of 1 m/s when the lower threshold was set between 30% and 42% of the peak DDM point. However, this method requires significant computation and manual work to build and maintain waveform libraries, and it is limited in extreme weather conditions or nonlinear retrieval problems.

The empirical modeling method is fast and efficient for estimating sea surface wind speed using statistical relationships or empirical formulas. It offers simplicity, efficiency, and practicality in real-time wind speed estimation compared to the waveform matching method. For example, Clarizia et al. [11] utilized empirical geophysical model functions (GMF) to retrieve wind speed based on various parameters such as mean, variance, Allan variance, leading edge slope (LES), and trailing edge slope (TES) of the DDM. They also developed a minimum variance estimator (MVE). Similarly, Rodriguez-Alvarez and Garrison [45] compared the MVE method with the maximum signal-to-noise ratio (SNR) method and the principal component analysis (PCA) method. The results indicated that the PCA method demonstrated better performance. In 2015, Foti et al. [12] proposed a wind speed retrieval algorithm based on the GNSS-R bistatic radar equation and SNR. They confirmed the significant capacity of low-cost, low-quality, and low-power GNSS-R receivers (e.g., ReSI) for global ocean wind speed retrieval at LEO heights. Furthermore, Bu et al. [46] classified the waveforms in DDM into three categories: center delay waveform (CDW), integral delay waveform (IDW), and differential delay waveform (DDW). They developed a composite wind speed estimation model using normalized bistatic radar cross-section (NBRCS) and LES observables, which resulted in an RMSE of 2.1 m/s and a determination coefficient of 0.906. This model exhibited improved accuracy and performance compared to traditional single-parameter models.

The retrieval of ocean surface wind speed is indeed a complex nonlinear problem influenced by various meteorological, oceanic, and geographical factors. While traditional empirical modeling approaches have their limitations in fully accounting for these complexities, intelligent optimization algorithms offer a more effective solution by incorporating global search and adaptive adjustment techniques to handle nonlinear and intricate problems. Guo et al. [47] proposed a novel approach using particle swarm optimization (PSO) for wind speed retrieval by combining the DDM observable with the MVE. The study highlighted that the PSO-based method showed dependencies on GPS constellation types and CYGNSS satellite identifiers, which differed from the MVE-based techniques.

Thanks to the development of computer technology, machine learning methods have further improved the processing of complex nonlinear problems in ocean wind speed retrieval, with their powerful nonlinear modeling capabilities that can capture complex nonlinear relationships and enhance the accuracy of ocean surface wind speed retrieval. Liu et al. [48] employed a multi-hidden-layer neural network (MHL-NN) to extract four different feature sets for ocean wind speed retrieval, resulting in significant improvement compared to traditional empirical models. Artificial neural networks (ANNs) enable fast completion of complex tasks by learning the relationship between inputs and outputs. Reynolds et al. [49] conducted the initial research on using ANN for wind speed estimation, Li et al. [50] evaluated the performance of ANN-based wind speed retrieval using CYGNSS data and analyzed the sensitivity of wind speed retrieval performance to different input parameters, finding that the geographical location of specular reflection points and the

height of uplift can significantly affect wind speed retrieval. To enhance the comprehensiveness of data input, Chu et al. [51] proposed an input composed of DDMs and all satellite receiver state (SRS) parameters. To effectively integrate the information of DDM and SRS, they introduced a heterogeneous multimodal deep learning (HMDL) approach that utilizes the heterogeneity of input data to retrieve wind speed. Asgarimehr et al. [52] developed an efficient wind speed retrieval method called CYGNSS net based on. Building upon this, Guo et al. [53] introduced a statistical correction convolutional neural network (CNN) with auxiliary information fusion. In this approach, the convolutional layers extract effective DDM features, and an adaptive polynomial form of cumulative distribution function matching is performed to eliminate bias. Bu et al. [54] presented an improved deep learning model called GloWS-Net, which significantly enhances the retrieval accuracy of high wind speeds compared to the CYGNSS net and MCNN models.

Liu et al. [55] utilized the characteristics of long short-term memory (LSTM) models in extracting temporal features from time series and proposed a recursive deep neural network (DNN) using feature attention mechanism (FA-RDN) for global ocean surface wind speed retrieval based on GNSS-R. However, FA-RDN only involves time-related input features for wind speed retrieval. Lu et al. [56] fully considered the spatiotemporal characteristics of ocean wind speed and put forward a hybrid CNN-LSTM network. Such a network can extract spatial features surrounding the specular point (SP) from the two-dimensional matrix of DDM through the CNN module, and extract temporal features from the time series through the LSTM module, thus better capturing spatiotemporal features and improving the accuracy of ocean wind speed retrieval. Nevertheless, the main challenge faced by deep learning models has been the poor performance of wind speed retrieval in high wind speeds due to the uneven distribution of wind speed samples. Therefore, future studies should select samples within a wider range of wind speeds to develop deep learning models for widely applicable spaceborne GNSS-R wind speed retrieval.

Table II summarizes and compares the methods for spaceborne GNSS-R sea surface wind speed retrieval, mainly focusing on the retrieval method, retrieval model, GNSS-R observables, retrieval accuracy, and advantages and disadvantages. The table only includes representative references, where “-” indicates that the information is not covered.

B. Sea Surface Wind Direction Retrieval

Both wind speed and direction are key factors for the ocean. Various techniques have been developed for determining sea surface wind speed and direction. Traditional methods consist of using microwave radiometers and scatterometers. Microwave radiometers estimate wind speed and direction by detecting changes in the roughness of the sea surface. On the other hand, scatterometers send out electromagnetic wave signals toward the ocean, receive reflected signals, from which can be applied to retrieve wind speed and direction.

As an emerging remote sensing technology, GNSS-R has also made significant progress in wind direction retrieval. Park

TABLE II
COMPARISON OF SPACEBORNE GNSS-R SEA SURFACE WIND SPEED RETRIEVAL METHODS

| Methods | Retrieval Models | Literature | GNSS-R Observables (Variables) | Retrieval Accuracy |
|-------------------------------------|---|------------------------|---|--|
| Waveform matching method | - | [44] | Normalized power value of DDM | 1–2 m/s for WS < 20 m/s |
| Empirical model method | Polynomial fitting | [57] | NBRCS, LES | For fully developed seas (FDS) GMF, the performance of the wind speed retrieval is below 20 m/s. The RMS difference is ~2 m/s at low wind speeds and grows to ~4 at 20 m/s. the component of that difference due to uncertainty in the CYGNSS wind speed retrieval is estimated to be 1.4 m/s. |
| | Exponential function | [12], [46] | DDMA, NBRCS, LES | ~2 m/s for WS < 20 m/s |
| | Power function | [14], [35] | NBRCS, DDMA, LES | RMS = 2.63 m/s, 2.04 m/s, and 1.77 m/s (vs. ECMWF, ASCAT, and buoys) |
| Combination of multiple observables | | [45] | Generalized Linear Observables (MSNR, MVU, and PCA) | When the WS is greater than 30 m/s, the PCA based RMSE is about 2.4 m/s lower than the MV estimator and about 0.2 m/s lower than the MSNR. |
| | Combination model based on MVE and PSO | [11], [47] | DDMA, DDMV, ADDMV, LES, TES, NBRCS | The RMS error in the MV estimator, at 1.65 m/s; PSO method is better than MVE method. The RMSE is better than 1.95 m/s for WS < 20 m/s. |
| Intelligent optimization algorithm | WS model based on ANNs (MHL-NN, ANN, MF-ANN) | [48], [49], [50] | DDMA, LES, incidence angle, NBRCS, GPS satellite number, RCG, etc. | The optimal RMSE of MHL-NN can reach 1.79 m/s; The RMSE of ANN are 1.58 m/s and 1.86 m/s respectively (vs. CYGNSS level 2 (version 2.1) WS products and buoys). |
| | WS model based on CNNs (HMDL, CYGNSSnet, MCNN, GloWS-Net) | [51], [52], [53], [54] | DDM BRCS, power_analog, effective scattering area, NBRCS, LES, etc. | The RMSE of MCNN is 1.53 m/s; The RMSE of CyGNSSnet is 1.36 m/s; The RMSE prediction accuracy of HMDL was improved by 36.8% (vs. traditional NN based solutions); The RMSE of the GloWS-Net model is 2.16 m/s. |
| Machine/Deep learning method | WS model based on LSTM (FA-RDN, CNN-LSTM) | [55], [56] | DDM BRCS, power_analog, effective scattering area, NBRCS, LES, SNR, RCG, etc. | The WS retrieval RMSE of the FA-RDN model can reach 1.45 m/s, 10.38%, 6.58%, 13.28%, 17.89%, 20.26%, and 23.14% higher than that of BPNN, RNN, ANN, RF, XGBoost, and SVR, respectively; The accuracy of the WS obtained by CNN-LSTM in terms of RMSE value is 1.34 m/s. |
| | WS model based on transformer (DDM-Former) | [58] | DDM BRCS, the corresponding effective scattering area, power analog CyGNSSnet, achieving an average RMSE of 1.43 m/s. | DDM Former outperforms traditional retrieval algorithms and CNN based baseline network CyGNSSnet, achieving an average RMSE of 1.43 m/s. |

1. MHL-NN represents a multi hidden layer neural network; ANN represents an artificial neural network; HMDL represents heterogeneous multimodal deep learning networks; CNN represents a convolutional neural network; MCNN represents the CNN with statistical correction; FA-RDN represents a recurrent neural network with feature attention mechanism; GloWS-Net denotes an improved deep learning framework; DDM-Former denotes Transformer networks; CNN-LSTM denotes a Hybrid Model Combining CNN and LSTM; MF-ANN denotes a Novel Artificial Neural Network.

and Johnson [59], [60] found that wind direction has higher sensitivity in nonspecular geometry compared to specular geometry, and the accuracy of wind speed retrieval plays an important role in the performance of wind direction retrieval. The retrieval can be carried out using DDM away from the specular part, and the outlook of wind retrieval using spaceborne GNSS-R is also proposed. Zhang et al. [61] realized the exploration of wind direction in nonspecular geometry by spaceborne GNSS-R on this basis, and provided the wind direction retrieval algorithm based on the delay-Doppler map average (DDMA) in nonspecular geometry. Simulation results show that spaceborne GNSS-R DDMA in nonspecular geometry can be used to retrieve the wind direction. Guan et al. [62] investigated the effect of different wind features in GNSS-R observables on the wind direction retrieval, and the results show that the wind direction retrieval performs better when the SNR and the metric angle are higher. Wang et al. [63] investigated the feasibility of retrieval of wind direction using low-level backward geometry of GNSS-R and focused on analyzing the effects of wind direction on sea surface roughness and scattering intensity.

In addressing the problem of spatial footprint blurring caused by Spaceborne GNSS-R receivers operating at high speeds in low orbits, Southwell and Inst [64] found that Spaceborne GNSS-R receivers operating at high speeds in low orbits lead to spatial footprint blurring. To address this problem, Gao et al. [65] introduced the concept of blurred gaze processing, which involves tracking multiple fixes simultaneously, to investigate the sensitivity of DDM to wind direction. They analyzed the relationship between multiple observations and wind direction and used a deep learning model for wind direction retrieval. Pascual et al. [66] investigated the effect of kurtosis of DDM samples in CYGNSS data on wind direction sensitivity and proved that CYGNSS data are sensitive to wind direction

$$\hat{\kappa} = A_0 + A_1 \cos(\text{WD}) + A_2 \cos(2\text{WD}) \quad (1)$$

where A_0 is the offset, A_1 is the upwind/downwind modulation factor, A_2 is the upwind/sidewind factor, and WD is the relative wind direction.

Zhang et al. [67] developed a support vector machine (SVM) model for sea surface wind direction retrieval using CYGNSS satellite data to address the difficulty of wind direction retrieval

in large space and large time span at the global sea surface, and the results show that the retrieval has a high classification accuracy in the dataset with wind speeds greater than 10 m/s, and the RMSE of the retrieval results is 26.70°. Zhang et al. [68] developed a sea surface wind direction retrieval model based on three machine learning algorithms (SVM, BP, and CNN) using CYGNSS L1 data. The results show that the CNN model outperforms the SVM model and BP model in retrieval of wind direction.

Future studies could improve the results of sea surface wind studies by using more high-quality data to provide more comprehensive and detailed information.

C. Applications: Hurricanes, Typhoons, and Tropical Cyclones Monitoring

Typhoon is a tropical cyclone, also known as hurricane, which is the result of the interaction between the atmosphere and the ocean. Typhoons are formed in tropical oceans and are characterized by strong winds and heavy rain. Monitoring a typhoon is of crucial importance for weather disaster prediction and warning, helping reduce the losses caused by typhoons.

GNSS-R has become one effective technique for typhoon monitoring [34]. It has the advantage of monitoring large-scale typhoon activities in real time and remotely without relying on traditional ocean buoys and aircraft detection. Martín et al. [69] and others used interferometric GNSS-R for typhoon monitoring. Li et al. [70] used the ocean reflection signals from the BeiDou geostationary orbit (GEO) satellites to conduct coastal typhoon observations. Through preliminary analysis of the BeiDou reflection signals collected in the experiment, the GNSS-R measured wind speeds match well with in situ data, and the average deviation was 1.6 m/s and an RMSE of 2.4 m/s. This promotes the application of the Beidou GEO satellites in typhoon monitoring. Ruf et al. [13] proposed to utilize the CYGNSS data to perform high temporal and spatial resolution wind speed observation to help predict the paths and intensities of typhoons. In addition, spaceborne data from the U.K. TDS-1 mission were successfully applied to typhoon monitoring, representing the first success of monitoring typhoons using spaceborne GNSS-R technique [71], [72]. Balasubramaniam and Ruf [73] constructed an empirical model considering azimuthal dependence by using the CYGNSS observation data and the wind speed data from the hurricane weather research and forecasting (HWRF) model for describing the variation of GNSS-R scattering cross sections in typhoons. It is found that the azimuthal dependence of the scattering cross section increases with wind speed, and changes in azimuthal direction can lead to a 2%–8% variation in the scattering cross section.

Understanding and predicting hurricanes is an important part of weather forecasting and climate research. Hurricanes and associated flooding and coastal inundation are among the most dangerous and expensive natural hazards for coastal communities. In addition, remote sensing of ocean surface winds usually lacks accuracy for very intense hurricanes. Shen et al. [74] used the ability of cross-polarized synthetic aperture radar (SAR) to detect wind speeds from hurricanes and found that wind

speed estimation with cross-polarized SAR has better accuracy compared to copolarized SAR. It provides valuable insights for numerical modeling of hurricanes, air-sea interaction, and climate change. Said et al. [75] employed simulated CYGNSS data to develop an algorithm for retrieving the maximum wind speed of a hurricane and compared the retrieved results with hurricane research reanalysis data (the best path) and the HWRF model data, with overall deviations relative to the optimal track of 11.3 and 2.1 m/s for optimal track maximum wind speeds less than 40 m/s and greater than 40 m/s, respectively.

Kim and Park [76] successfully monitored changes in water levels caused by hurricane-induced storm surges through the analysis of multifrequency and multisystem GNSS. By using spectral analysis and statistical data processing of multifrequency GNSS signals, their method was able to detect the effects of storm surges on water levels, improving the accuracy and temporal resolution of GNSS-R water level measurements. The proposed algorithm was validated through a case study of the storm surge during Hurricane Harvey in 2017, with results showing that the correlation coefficient between GNSS-R measurements and tide gauge readings at the same location was 0.97.

Wang et al. [77] proposed a joint use of spaceborne microwave sensors and the CYGNSS constellation to observe tropical cyclones. The TC tracks obtained by this method were compared with the best tracks provided by the National Hurricane Center, with mean absolute error values ranging from 18.4 to 46 km and standard deviation varying between 15.1 and 28.2 km. Morris and Ruf [78] developed a method for estimating the integrated kinetic energy of tropical cyclones using CYGNSS observations, demonstrating the validity and feasibility of the method through testing and evaluating performance with simulated data. Morris and Ruf [72] also utilized CYGNSS satellite observations to estimate the surface wind speed structure and intensity of tropical cyclones. Mayers and Ruf [79] proposed a new method to determine the TC center location using wind speed measurements from CYGNSS. The storm center location is estimated by fitting a parametric wind model to the CYGNSS surface wind speed data, where the wind speed as a function of radius is described as

$$V(r) = \frac{2r(R_m V_m + 0.5f R_m^2)}{R_m^2 + ar^b} - \frac{fr}{2} \quad (2)$$

where r is the distance from the storm center, f is the Coriolis factor, R_m is the radius of maximum winds, and V_m is the maximum wind speed. The factor a can be solved from the other factors by requiring that the maximum value of $V(r)$ equal V_m . The exponent b controls the rate at which the winds radially decay away from the inner core.

On this basis, Ruf et al. [80] evaluated the CYGNSS ocean surface wind speed measurements in terms of uncertainty, dynamic range, sensitivity to precipitation, spatial resolution, spatial and temporal sampling, and data latency. They found that the average revisit time of CYGNSS satellites was 9.1 h, and the spatial coverage reached 50%, which satisfied the mission's threshold requirements.

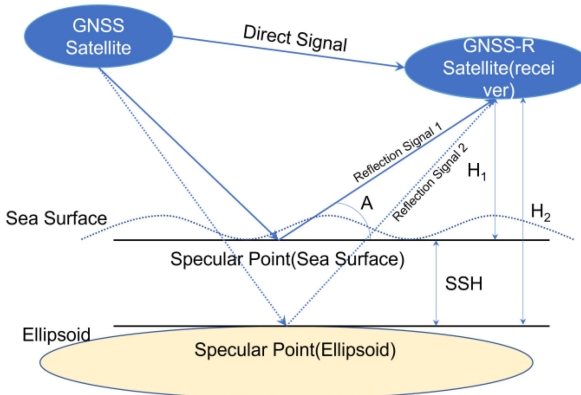


Fig. 1. Geometric principles of spaceborne GNSS-R altimetry [82].

However, it is worth noting that the current spatial resolution of Spaceborne GNSS-R data may not be sufficient for monitoring small-scale weather phenomena such as hurricanes. The development and progression of hurricanes often happen on a smaller spatial scale. Therefore, it is recommended to consider generating higher resolution data in the future to accurately monitor the location, intensity, and trajectory of hurricanes.

IV. SEA SURFACE ALTIMETRY AND WAVE HEIGHT RETRIEVAL USING SPACEBORNE GNSS-R

A. Sea Surface Altimetry

The measurement of SSH holds great importance in fields such as ocean meteorology, ocean engineering, and marine scientific research. The traditional approach involves using tidal gauges, which require the consideration of altimeter deviations and drift to calculate the variation in sea level over time [81]. However, altimeters are expensive and susceptible to environmental influences. Alternatively, GNSS-R-based retrieval has become a commonly used method due to its advantages of low power consumption, cost-effectiveness, and high spatial resolution. Martin-Neira [6] pioneered the use of GNSS-R for SSH measurement in 1993. The geometric principle of spaceborne GNSS-R altimetry is depicted in Fig. 1.

There are two commonly used methods for measuring SSH using ground-based GNSS-R techniques. The first method is the GNSS interferometric/multipath method, which involves analyzing the interference or multipath effect of GNSS signals. This method utilizes the SNR obtained by the receiver to measure SSH [83]. Purnell et al. [84] proposed a modeling technique based on SNR data to estimate the accuracy of GNSS-R sea level measurements and analyze measurement uncertainty.

The second method is the conventional GNSS-R (cGNSS-R) method, which retrieves SSH by observing the time delay between reflected and direct GNSS signals. There are two approaches for measuring the time delay: code-based methods and carrier-based methods. Code-based methods track the code phase of the reflected and direct signals to determine the time delay [85], [86], while carrier-based methods track the carrier phase to achieve the same objective [87]. Cardellach et al. [39] introduced the first grazing angle (GA) carrier phase-delay

method for SSH retrieval. However, the carrier-based method requires continuous carrier phase and strong coherent components in the reflected signal, imposing smoothness requirements on the reflecting surface. This limits its application in ocean surveying. In contrast, code-based methods have lower requirements for signal coherence, making them more widely applicable.

Ground and airborne GNSS-R technologies have provided the basis for the development of spaceborne GNSS-R systems [88], [89]. The U.K.-DMC satellite constellation launched in July 2014 was the first to carry a GNSS-R receiver capable of generating a differential DDM containing information about delay and Doppler around the SP.

Subsequently, some researchers conducted sea surface altimetry studies using TDS-1 data. Song et al. [90] conducted high-resolution processing of Doppler and code delay based on raw data from the TDS-1 satellite and explored the potential of using higher time sampling rates to improve accuracy using two different height measurement methods. Mashburn et al. [91] used GNSS-R data from the TDS-1 satellite for sea surface altimetry and developed an error budget by analyzing the sources of error. The SSH residual was found to be 6.4 m with a 1σ integration time of 1 s compared to the mean sea surface topography. For accurate delay retracking, correction for ionospheric effects, and spacecraft receiver positioning in GNSS-R altimetry studies, Mashburn et al. [92] also utilized a simulated DDM to match with the measured data in order to obtain accurate specular reflection delays through correcting the path delay effects in conjunction with a global ionospheric map (GIM). This method, which is based on reflection modeling and ionospheric correction, is able to extract more accurate sea surface altimetry information from GNSS-R measurements, providing new possibilities for related applications.

Li et al. [93] utilized raw IF data collected by CYGNSS satellites to comprehensively analyze the high performance of oceanographic measurements with spaceborne GNSS-R technology. They calculated the ellipsoidal height of the sea surface above the WGS84 ellipsoid using the double-base geometry [6]

$$H_e^{\text{obs}} = -\frac{c\tau_{\text{rtrk}}^{\text{obs}} - (\delta\rho_{\text{iono}} + \delta\rho_{\text{tropo}} + \delta\rho_{\text{bl}})}{2 \cos i} \quad (3)$$

where i is the angle of incidence, $\tau_{\text{rtrk}}^{\text{obs}}$ is the residual two-base delay derived from different retrackers, $\delta\rho_{\text{iono}}$ is the ionospheric delay correction term, $\delta\rho_{\text{tropo}}$ is the tropospheric two-way tilt delay, and $\delta\rho_{\text{bl}}$ is the antenna baseline correction.

Due to the limited capabilities of some satellite missions, Nguyen et al. [94] used the dual-frequency GPS reflection signal data collected by the Spire satellite constellation for the first time to construct a phase height retrieval model, as shown in formula (4), achieving centimeter-level high-precision height estimation in sea ice covered areas and open sea areas

$$\delta h = \frac{\hat{\rho} - \rho}{2 \sin \alpha} \quad (4)$$

where δh represents the surface height deviation from a reference surface, ρ represents the observed geometric distance of the reflected signal path, $\hat{\rho}$ represents the prior distance of the

signal path based on the reference surface, and α is the angle between the local tangent plane of the SP and the line-of-sight to the transmitter.

The launch of China's BF-1 satellite and FY-3 satellite has significantly enhanced spaceborne GNSS-R observations. The utilization of multiple constellations of GNSS signals, which exhibit differences in signal performance based on frequency bands and modulations, can improve the accuracy of height measurements [95]. Due to the highly nonlinear complexity of the sea surface, traditional empirical models often fail to fully consider the effects of various factors. In contrast, machine learning and deep learning techniques have proven to be effective in data processing. However, compared to applications such as sea surface wind speed retrieval and soil moisture detection, machine learning and deep learning for spaceborne GNSS-R sea surface altimetry are still in their early stages with limited studies conducted thus far. Zhang et al. [82] proposed the use of machine learning methods, such as principal component analysis combined with support vector regression (PCA-SVR) and CNN, for obtaining SSH based on TDS-1 data. They further validated and compared the performance of these methods. In addition, Zhang et al. [96] developed two different CYGNSS SSH retrieval models based on widely used machine learning techniques, including backpropagation neural network (BPNN) and CNN.

To improve the accuracy of sea surface height retrieval, Wang et al. [97] proposed a novel weighted average fusion feature extraction method. Built on this research, an end-to-end modified residual multimodal deep learning method was introduced, which leverages complete DDM information to further enhance the retrieval accuracy of SSH [98]. However, most studies have mainly focused on postprocessing strategies to improve performance without considering practical (near) real-time applications. To address this challenge, Liu et al. [99] proposed a cloud service-based approach for near real-time sea level measurements using a robust Kalman filter to achieve high accuracy and temporal resolution. The results show negligible bias compared to retrieval in postprocessing mode, confirming the practical significance of the proposed method for real sea level monitoring applications. Table III summarizes and compares methods for spaceborne altimetry of the sea surface, mainly focusing on retrieval methods, observational data, retrieval models, observed values, retrieval accuracy, and validation models. The table lists only representative references, with “-” indicating aspects not covered.

The marine environment is a complex and dynamic system that is influenced by various factors. The complexity and uncertainty involved make it challenging to accurately predict future SSH. In practical applications, it is necessary to synthesize, validate, and evaluate multiple methods and data sources to enhance the accuracy and reliability of prediction results. Further research and technological advancements are needed to overcome this challenge.

B. Sea Surface Significant Wave Height Retrieval

The SWH of ocean waves is an important parameter that describes wave energy and has a significant impact on the marine

environment and maritime activities. Sea surface roughness and scattering coefficient are important factors that affect the reflection signal of spaceborne GNSS-R [102]. The dual-scale model (TSM) is a reliable method for analyzing electromagnetic scattering from the sea surface. TSM divides the sea surface into two parts: large-scale roughness and small-scale roughness. It uses the following formula to define the scattering coefficient [103]:

$$\sigma_{\text{TSM}} = \sigma_{\text{KA-GO}} + \sigma_{\text{SPM}} \quad (5)$$

where $\sigma_{\text{KA-GO}}$ represents the large-scale surface roughness scattering coefficient calculated based on the Kirchhoff approximation-geometric optics (KA-GO), primarily related to swell. σ_{SPM} represents the small-scale surface roughness scattering coefficient calculated using the small perturbation method (SPM), mainly associated with wind waves. SWH represents the average height of the highest third of ocean surface waves generated by wind and swell. When sea surface wind speed is low, swell contributes predominantly to SWH [104]. Conversely, in high wind speed conditions, wind waves are the primary components of SWH.

To accurately measure SWH, researchers have explored various retrieval methods. This section provides a brief overview of some common methods for SWH retrieval, discussing their characteristics and limitations.

Buoy observation is a widely used SWH retrieval method with high accuracies. However, its application is limited due to the high cost and restricted coverage of buoy equipment, which makes it challenging to implement in large-scale sea areas [105]. Satellite altimetry is another commonly used method for measuring ocean wave parameters. However, due to the limited resolution of satellite observations, it can be difficult to obtain detailed results [106]. Interference complex field (ICF) is a method that calculates SWH by utilizing the effective correlation time function of coastal GNSS reflected signals and direct signals [107]. Alonso-Arroyo et al. [108] conducted an analysis of oscillation frequency and coherence loss using the interference pattern technique (IPT) and retrieved SWH and mean sea surface level with ground experiment data. IPT is not applicable to spaceborne GNSS-R scenarios [109], although there are special cases where this pattern occurs. When the relative delay between the direct GNSS signal and the reflected signal is less than the code-slice length (e.g., about 300 m for C/A codes), both signals contribute to the correlation sum amplitude computed by the receiver, and an IPT-like signaling pattern occurs. This situation has been found in GNSS-RO measurements where the receiver is not stationary [100]. However, in spaceborne GNSS-R applications, the IPT method is not applicable due to the large satellite-terrestrial path variations [109], where the relative delays of the direct and reflected signals usually exceed the code-slice length.

Qin and Li [110] proposed a multisatellite observation SWH retrieval method based on GNSS-R. This algorithm employs DDM to extract SNR and introduces offset correction for elevation differences to retrieve SWH. However, this method is only applicable when SWH is below 2.5 m. Clarizia et al. [11] proposed using the LES of the IDW to retrieve SWH, but further

TABLE III
COMPARISON OF SPACEBORNE SEA SURFACE ALTIMETRY METHODS

| Method | Literature | Data | Retrieve Models | Observables | Precision | Verification Model |
|-----------------------------------|------------|----------|----------------------------|--|---|--|
| Bistatic group delay (code phase) | [95] | CYGNSS | Formula (3) | HALF (the point at a fraction of the peak power), DER (the point with the maximum of waveform's first derivative), and FIT (fitting the waveform to its model) | Two-way ranging precision can reach up to 3.9 and 2.5 m | |
| | [92] | CYGNSS | Formula (3) | DDM | The RSS residual error of the CYGNSS altimetry observations is estimated to be 6-m delay at the average observed CYGNSS SNR using VZ18DDM tracking on 1-s observations. | |
| | [91] | TDS-1 | Quasi-spherical Earth mode | DDM | Compared with the average sea surface topography, the residual ssh is 6.4 m and the 1σ integration time is 1 s. | |
| | [90] | TDS-1 | Formula (3) | Code Phase | When the time resolution is 0.2, 0.5, and 1 s, the precision of the code phase altimetry can reach 1.01 m, 0.67 m, and 0.51 m, respectively. | DTU (Danmarks Tekniske Universitet) models |
| Carrier phase-delay | [100] | GPS LEO | - | IPT | Obtain a vertical accuracy of 0.70 meters under horizontal sampling of ~1 km | |
| | [39] | CYGNSS | - | Carrier phase-delay measurements | The combined precision, is 16/20 cm (median/mean) precision at 50 ms integration (a few centimeter level at 1 Hz). | |
| | [94] | Spire | Formula (4) | Dual-frequency reflection signals (Phase and pseudo range measurements) | Compared with the sea surface model, the accuracy after removing the average height difference is 3 cm | |
| | [101] | BuFeng-1 | - | DDM and GNSS-R variables | The results were compared to the DTU18 20 min product with RMSD and R^2 of 0.94 m and 99.15%, respectively. | |
| Machine learning | [82] | TDS-1 | PCA-SVR and CNN | DDM and GNSS-R variables | The MAE, RMSE and R^2 of the PCA-SVR retrieval model are 0.61 m, 1.72 m, and 99.56%, respectively; and the MAE, RMSE, and R^2 of the CNN retrieval model is 0.71 m, 1.27 m, and 99.76%, respectively. | |
| | [96] | CYGNSS | BP and CNN | DDM and GNSS-R variables | The MAE of 1.04 m for the BP model and 0.63 m for the CNN model. | |

research on SWH retrieval has not been conducted. Peng and Jin [109] estimated the global ocean SWH using spaceborne CYGNSS GNSS-R data and the relationship between the square root of CYGNSS DDM SNR data and SWH. Yang et al. [111] estimated SWH using a polynomial function relationship between SWH and the DDMA as well as the LES of CYGNSS data developed based on the ERA5 data. Bu and Yu [112]

achieved relatively good results by retrieving SWH using the GMF with CYGNSS data, which confirms the feasibility of estimating SWH using spaceborne GNSS-R. To improve the accuracy of SWH retrieval, Wang et al. [113] adopted a multivariate regression machine learning model, which introduced additional input variables in an attempt to capture more factors that affect SWH to improve the accuracy and reliability of the

model. Multiple models were compared and evaluated to select the best model and further improve the SWH retrieval method. Wang et al. [114] compared the effectiveness of the GMF and NN model in retrieving SWH. The results demonstrated that the NN model outperformed traditional GMFs. NN models possess greater flexibility and nonlinear modeling capabilities, allowing them to accurately capture the complex relationship between SWH and input variables. Bu et al. [115] proposed for the first time a joint retrieval method suitable for spaceborne GNSS-R sea surface rainfall and wind waves, establishing a deep convolutional neural network (DCNN) model to estimate SWH of rain and wind-driven sea conditions. The research results indicate that deep learning methods have great potential in SWH retrieval. However, wind speed and swell are the main interfering factors affecting precipitation retrieval, and eliminating or mitigating the impact of wind speed and swell on precipitation intensity retrieval is a key challenge that needs to be addressed in the next step.

Table IV summarizes and compares different sea surface SWH retrieval methods for GNSS-R. We mainly compare the methods used, GNSS-R data, GNSS-R observations, retrieval models, and retrieval accuracy. “-” indicates not involved. From the table, it can be seen that the research on GNSS-R wave SWH retrieval mainly focuses on shore-based, ship-based, and spaceborne experiments. For spaceborne GNSS-R SWH retrieval, the main focus is on building empirical models for SWH retrieval based on GNSS-R observation values. Although some promising results have been achieved, due to the fact that empirical models only consider a limited number of variable parameters, there are significant challenges in constructing multivariate regression models considering multiple factors, resulting in low robustness and retrieval accuracy of the model, making it difficult to apply in practice. Although machine learning algorithms, such as stepwise linear regression, SVM, ANN, sparrow search algorithm extreme learning machine, and bagged tree (BT) have proven to have advantages in constructing multivariate regression SWH retrieval models and have higher retrieval accuracy than empirical models, the input data of the model often ignore key feature information in DDMs. This limits the accuracy of SWH retrieval. Deep learning methods, such as DCNNs, have been proven to be effective for retrieving SWH from spaceborne GNSS-R data. DCNNs can automatically extract feature information related to sea surface SWH from BRCS DDM and effective scattering area, and excel in automatically extracting complex spatial features from multiple input images. However, this method ignores the characteristics of time series.

Therefore, future research should focus on developing hybrid models that take into account both spatial and temporal correlation feature information. One possible solution is to construct a hybrid model that integrates DCNN and bidirectional LSTM to improve the performance of global SWH retrieval for spaceborne GNSS-R.

C. Sea Surface Swell Height Retrieval

Sea swell is an important type of marine meteorology and its formation process is influenced by various factors such as wind,

seawater density, temperature, rainfall, and bed characteristics. Swells have a wide range of impacts on the ocean and coastal areas, directly threatening the safety of ships at sea and the stability of offshore structures.

Unlike wind waves, swells are typically waves that propagate from distant wind fields and continue to move without being influenced by local winds. Swells can be modeled as narrowband Gaussian processes, and the swell spectrum model is as follows [121]:

$$\psi_{\text{swell}}(k_x, k_y) = \frac{\langle h^2 \rangle}{2\pi\sigma_{kx}\sigma_{ky}} \exp \left\{ -\frac{1}{2} \left[\left(\frac{k_x - k_{xm}}{\sigma_{kx}} \right)^2 + \left(\frac{k_y - k_{ym}}{\sigma_{ky}} \right)^2 \right] \right\} \quad (6)$$

where $\langle h^2 \rangle$ represents the variance of wave height, σ_{kx} and σ_{ky} represent the standard deviation of wave spectrum, k_x and k_y , respectively, represent the components of wave number k in the x and y directions, k_{xm} and k_{ym} , respectively, represent the peak wave numbers of swell waves in the x and y directions. $k_m = \sqrt{k_{xm}^2 + k_{ym}^2} = \frac{2\pi}{\Lambda_m}$, Λ_m is 400 m, and $\sigma_{kx} = \sigma_{ky} = 0.0025 \text{ m}^{-1}$ [122].

Swells are usually associated with large-scale rough sea surfaces that have a significant impact on GNSS sea surface reflection signals, and the impact of swells is more significant at low wind speeds. When retrieving wind speed under such conditions, the presence of swells can introduce substantial retrieval errors, thus reducing the accuracy of wind speed retrieval.

Traditional swell measurement is accomplished via collecting sea surface information by placing buoys on the sea surface, which has some limitations, including limited coverage, high cost, and susceptibility to environmental factors. In contrast, using satellite altimeters for observation has the advantage of covering a global range. Albuquerque et al. [123] used satellite altimeter data to correct sea breeze and swell data, but the accuracy may be limited due to the limited spatial resolution of satellite altimeters. Li [124] utilized spaceborne SAR images to monitor the height of the swell. Altiparmaki et al. [125] proposed using SAR altimetry data to detect swells by studying the spectrum of fully focused SAR altimetry data. However, due to the sparse data obtained in both time and space, constructing an accurate model can be challenging. Several studies have focused on the use of high-frequency radar (HFR) for swell measurements [126]. HFR is usually a land-based radar that monitors sea surface conditions up to 300 km from the coast. With a spatial resolution of 0.5–5 km and a temporal resolution of about half an hour, it is capable of continuously acquiring real-time sea information [127], [128].

In addition, with the development of GNSS technology, GNSS-R as a new remote sensing technology has the advantages of a short revisit period, low observation cost, and high spatial and temporal resolution. Bu et al. [129] used spaceborne GNSS-R data from eight CYGNSS satellites to retrieve swell height. In order to improve the accuracy of its retrieval, an improved hybrid optimization algorithm was proposed based on

TABLE IV
COMPARISON OF GNSS-R SEA SURFACE SIGNIFICANT WAVE HEIGHT RETRIEVAL METHODS

| Method | Literature | GNSS-R Data | Reference Data | GNSS-R Observations | Retrieve Models | Precision |
|--------------------------------|--------------|--|---|---|--|---|
| ICF | [107] | Measured shore-based GPS-R data | Buoy data | correlation time | A semi empirical model on correlation time and SWH | — |
| Interferogram Technology (IPT) | [108] | SMIGLOL Reflectometer Measurement Data | VEGAPULS62 radar measured SWH data | Elevation mask | logarithmic function | When SWH<0.8 m, the retrieval accuracy of SWH reaches 6 cm. |
| Upper cut-off elevation method | [116] | Shore-based GNSS-R | — | Upper cut-off elevation | Generalized shallow water wave growth model | A correlation coefficient > 80% between WS measurements and SWH retrievals. |
| | [117] | Shore-based GNSS-R data | Datawell's Directional Waverider buoy (Datawell DWR-MkIII) | SNR | multinomial | The average absolute percentage error, RMSE, and maximum error are 8.26%, 0.1671 m, and 0.32 m, respectively. |
| | [114] | Shipborne GNSS-R | Shipborne meteorological station SWH; ERAS and Jason-3 SWH | Correlation time; spectral width; peak frequency | GMF and NNs | The RMSE of SWH retrieval is 0.38 m. |
| | [118] | Shipborne GNSS-R | Observation data of nautical seismometer and maritime wavemeter | Time delay window | multinomial | The correlation coefficient is 0.97, and the RMSE is 0.22. Compared with ECMWF data, the standard deviation and correlation coefficient of SWH retrieval are 0.2153 m and 0.9752, respectively. |
| | [109] | CYGNSS | ECMWF, AVISO, buoy data | SNR | power function | Compared with ECMWF data, the RMSE and correlation coefficient of SWH retrieval are better than 0.257 m and 0.945, respectively. |
| Empirical modeling method | [111] | CYGNSS | ECMWF, AVISO, buoy data | DDMA, LES | N-order polynomial | Compared with ECMWF data, the RMSE and correlation coefficients of SWH retrieval are better than 0.257 m and 0.945, respectively. |
| | [112], [119] | CYGNSS | ECMWF | DDMA; NIDW LES; NIDW TES; NCDW LES; NCDW TES; NCDW LEWS | Power function; Binomial exponential function | Compared with ECMWF data, the RMSE and correlation coefficients of SWH retrieval are 0.503 m and 0.88, respectively. The RMSE and correlation coefficient (CC) of the combined model are better than 0.428 m and 0.91, respectively, which is 14.74% higher than the RMSE of the LES observation model. |
| | [120] | CYGNSS | ECMWF | DDMA; NIDW LES | Two term exponential function; MVE based combination model | The RMSE and correlation coefficient (CC) of the combined model are better than 0.428 m and 0.91, respectively, which is 14.74% higher than the RMSE of the LES observation model. |
| Machine learning methods | [113] | CYGNSS | ECMWF; NDBC Buoy | DDM-related variables and auxiliary variables | stepwise linear regression, Gaussian SVM, ANN, sparrow search algorithm-extreme learning machine, and BT | The BT model performs best, with RMSE and correlation coefficient of 0.48 m and 0.82, respectively. |
| Deep learning methods | [115] | CYGNSS | ECMWF | Power analog DDM, DDM-related variables and auxiliary variables | DCNN | The RMSE of SWH retrieval is better than 0.20 m. |

TABLE V
COMPARISON OF SEA SURFACE SWELL HEIGHT RETRIEVAL METHODS

| Method | Literature | Data | Reference Data | Retrieve Models | Precision |
|---------------------------|------------|---|--|---------------------------------------|--|
| Satellite Altimeter | [123] | Bathymetry and distance from land | bouy data | Multiple linear regression model | The swell has achieved a 5% improvement in SI. |
| Spaceborne SAR | [124] | ASAR wave mode data | bouy data | - | The RMSE of ASAR wave peak direction compared to buoy measurement is 17°. |
| Shore-based HFR | [131] | VHF radar data | situ data | - | RMS differences relative to in situ wave height measurements range from 0.16 to 0.25 m as the radar beam angle increases from 22° to 56°. |
| X-band Radar | [132] | The X-band marine radar sea surface images. | Buoy data | Ensemble empirical mode decomposition | The root mean square differences compared to the buoy reference is 0.36 m. |
| Spaceborne GNSS-R methods | [129] | CYGNSS | ECMWF reanalysis swell height datasets | SA-PSO algorithm | The RMSE of the SA-PSO method is improved by 23.53%, 26.42%, 30.36%, and 7.14%, respectively. The RMSEs of SWH retrieving for swell and wind waves are greater than 0.394m and 0.397m, respectively, with a correlation coefficient R of 0.90. |
| | [130] | CYGNSS | ERA5, WaveWatch III | DCNN | |

the PSO algorithm [47] (i.e., a combination algorithm combining simulated annealing (SA) and PSO, SA-PSO). The experimental results showed that the estimated swell height of the proposed method was consistent with reference data (i.e., ERA5 swell height). However, the empirical model constructed in this study only considers a limited number of input variable parameters, thereby limiting the retrieval accuracy of swell height. Swell changes are complex and cannot be adequately characterized by simple models. Therefore, the development of more advanced models becomes necessary. Machine learning or deep learning techniques offer significant advantages in modeling complex variable relationships. Consequently, Bu et al. [130] became the first to apply deep learning methods to estimate swell height using spaceborne GNSS-R data. The study also discussed the performance of machine learning models in swell height retrieval. Experimental results indicate that the proposed DCNN model outperforms other models when ERA5 serves as the reference data. However, as the swell height increases, the retrieval performance of the model gradually decreases, especially when the swell height is greater than 3 m. At this point, there is an underestimation of the swell heights retrieved by all eight models. The underestimation may be due to two key factors: 1) the sensitivity of DDM observables reaches saturation during high swell; 2) the distribution of swell height data is extremely uneven. Throughout the entire training process, due to the presence of a large amount of data distribution related to medium swell heights, all eight models tend to conservatively predict within the range of high swell heights. Therefore, the retrieval performance in the high swell range needs to be further improved in the future. In addition to the content introduced here, Bu et al. [130] also reported more detailed information on the impact of rainfall on swell height, model retrieval performance under different sea state conditions, and other aspects.

Table V summarizes and compares different methods for sea surface swell height retrieval. A comparison is made mainly in terms of the methods used, data, reference data, retrieval model, and retrieval accuracy. “-” indicates not applicable. Only representative literature is listed in the table.

Meanwhile, in future research on swell height, deep learning is still in the development stage in the GNSS-R field but they have great potential for development in the research of swell retrieval.

D. Applications: Tsunamis and Storm Surge Detection

Sea surface wind mapping, wave height measurement, and altimetry have been demonstrated applications; the use of spaceborne GNSS-R for tsunami detection is a potential application but has not been confirmed with field data yet.

A tsunami is a natural disaster characterized by large ocean waves triggered by underwater geological activities, such as earthquakes, volcanic eruptions, landslides, or other similar events. To mitigate the impacts of tsunamis, it is crucial to monitor them in real-time and provide timely and accurate information for emergency response and protective measures to minimize human and coastal damage.

Tsunami monitoring requires continuous surveillance of potential tsunami activities in the ocean using certain technical methods. Existing methods include underwater seismic monitoring [133], seawater level monitoring [134], and marine meteorological monitoring [135]. Through these monitoring approaches, essential data and information such as earthquake parameters, sea level changes, meteorological conditions, acoustic signals, and sea surface conditions can be obtained for timely detection and warning of tsunamis.

Initially, early tsunami monitoring relied on water level measurement instruments placed in coastal areas, such as buoys. However, this approach is expensive and covers only limited areas. Satellite altimeters offer accurate tsunami monitoring capabilities, but their longer revisit cycles introduce potential delays in warning. With the continuous advancement of technology, modern tsunami monitoring systems have become more sophisticated and comprehensive. Spaceborne GNSS-R technology offers a promising alternative for detecting tsunamis and estimating tsunami parameters.

Stosius et al. [136] conducted a comparison between the meshed comb constellation and the Walker constellation layout and found that the Walker constellation provides a much more evenly distributed reflection point coverage compared to the meshed comb constellation. If Spaceborne GNSS-R is capable of detecting tsunami waves 20 cm or higher, the 48/8 or 81/9 Walker constellations can accurately detect strong tsunamis with a magnitude (M) of ≥ 8.5 from any orbital altitude within 15–25 min.

Furthermore, Stosius et al. [137] analyzed the detection performance of a GNSS-R constellation using signals from GPS, GLONASS, and Galileo at an altitude of 900 km and an inclination of 60° . They utilized the TUNAMI-N2 wave propagation model to determine the probability of tsunami detection by calculating the number of simulation runs in which a tsunami was detected within a specific time period. The results indicated that the best detection performance was achieved when all three signals from GPS, Galileo, and GLONASS were combined.

DDM data reflect changes in the surface scattering scenario, which include ocean surface waves and surface disturbances caused by tsunamis. Yan and Huang [138] proposed a simulation method for tsunami detection and parameter estimation based on GNSS-R DDM. This method utilized the double static scattering Z-V model, Cox and Munk sea surface mean square slope model, and wind disturbance model caused by tsunamis. To validate the applicability of the Cox and Munk models in tsunami scenarios, the consistency between the Cox and Munk models based on the scattering coefficient and Jason-1 measurement results was compared. The correlation coefficient was found to be 0.93, confirming the suitability of the Cox and Munk models in tsunami scenarios.

In 2016, Yan and Huang [139] employed the two-antenna scattering interferometry method to extract the sea surface scattering coefficient from DDM data. They also retrieved the distribution of sea surface wind velocity based on the scattering coefficient. In addition, they proposed a method to determine sea surface height anomaly (SSHA) results and detect tsunamis in order to reduce the false alarm rate. Through comprehensive simulation tests, the accuracy and feasibility of the scheme were verified. The processes of SSHA measurement and tsunami detection caused by tsunamis are illustrated in Fig. 2. In Fig. 2, σ_0 is the scattering coefficient, A is the tsunami SSHA amplitude, k is the tsunami SSHA undirected wave number, and φ_0 is the tsunami SSHA phase shift.

In the same year, Yu [140] proposed a method to detect weak tsunamis using noise SSH measurement data. The method involves comparing simulated data with actual data and utilizing a

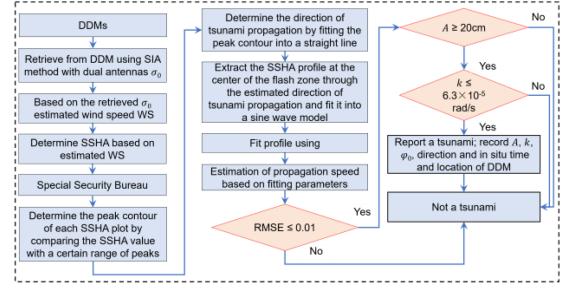


Fig. 2. Flowchart of SSHA measurement and tsunami detection caused by tsunami [139].

trigonometric function model to describe the shape of the leading wave of a tsunami. In addition, a detection method based on bin averaging (BA) technology is proposed for determining the presence of a tsunami through hypothesis testing. The formulas for the probability of detection (PD) and the probability of false alarm (PFA) are derived as

$$\text{PD} = \beta(\gamma, s_{\text{tw}}^{(1)}) + \sum_{j=2}^k \left(\prod_{i=1}^{j-1} m(\gamma, s_{\text{tw}}^{(i)}) \right) \beta(\gamma, s_{\text{tw}}^{(j)}) \\ = 1 - \prod_{i=1}^k m(\gamma, s_{\text{tw}}^{(i)}) \quad (7)$$

$$\text{PFA} = \left(1 + \sum_{j=2}^k \left(\prod_{i=1}^{j-1} m(\gamma, s_{\text{tw}}^{(i)}) \right) \right) \alpha(\gamma) \quad (8)$$

where $s_{\text{tw}}^{(i)}$ is the tsunami component (s_{tw}) of the i th BA output, PFA is the probability that the hypothesis of presence of a tsunami is accepted, the threshold γ can be determined by giving the PFA denoted by α , $\beta(\gamma, s_{\text{tw}})$ is the probability that the hypothesis of presence of wave is accepted when the wave is present, and $m(\gamma, s_{\text{tw}})$ is the probability that the hypothesis of absence of wave is accepted but a wave is present.

On this basis, Yu [141] estimated the wave height and wavelength of a tsunami based on GNSS-R SSH measurements. By processing and analyzing GNSS-R observation data, the waveform and parameter estimation of the tsunami can be obtained. In addition, a simplified parameter estimation method was proposed to evaluate the estimation performance of tsunami wave height and wavelength using the Cramer–Rao lower bound, and the wave height and wavelength can be clearly defined. In another study, Kim et al. [142] analyzed event-driven water level changes and used GNSS reflection measurement technology to monitor tsunamis and storm surges. Through an improved GNSS-R data processing method that included using multiband GNSS signals, determining the optimal processing window, and employing Kalman filtering to determine altitude, they successfully detected two tsunami events and two storm surge events. The correlation coefficients with nearby tide meters were high, with values of 0.944, 0.933, 0.987, and 0.957, respectively. These results highlight the significant potential of monitoring tsunamis and storm surges using GNSS-R technology.

Storm surge refers to an abnormal rise in water level in the ocean caused by storms or climate systems. It is primarily a result of strong winds and low-pressure systems, combined with tidal effects, leading to a significant increase in sea level. Storm surges can have a devastating impact on coastal communities, ports, shipping, fisheries, and coastal ecosystems, resulting in extensive damage.

Detecting storm surges requires real-time attention to changes in water level and sea surface wind speed. Ocean observation stations established in coastal areas are usually equipped with water level measurement equipment, meteorological stations, buoys, and other sensors, which can record data such as wind speed, direction, pressure changes, and SSH.

As storm surge leads to an abnormal increase in water level, analyzing the reflected signal characteristics of GNSS signals can provide information about the abnormal increase in seawater level caused by storm surge. Two commonly used analytical methods for GNSS water level analysis are the phase-delay analysis method and the SNR analysis method [143]. In the SNR analysis method, before a reflected signal is received, it undergoes multiple paths. These multiple paths result in delay differences between the reflected signals and the direct signal, introducing interference patterns. The SNR analysis method can be applied to the detection of storm surges using spaceborne GNSS-R, and the SNR is represented by the following equation [142]:

$$\text{SNR}^2 = A_d^2 + A_m^2 + 2A_d A_m \cos(\psi) \quad (9)$$

where A_d and A_m are the amplitudes of the direct and multipath signals, respectively, and ψ is the phase difference between the two signals.

Vu et al. [144] utilized blind signal decomposition techniques such as singular spectrum analysis and continuous wavelet transform to extract storm features of SSH from GNSS-R tidal data. This approach offers a new perspective and tool for studying storm surges, enabling a deeper understanding and prediction of their behavior and impact. Peng et al. [145] were pioneers in applying GNSS interferometric reflection measurements to detect storm surges. By analyzing the SNR data of GNSS signals, they obtained sea level measurements that were validated against traditional tidal meter data (with an RMS difference of approximately 12.6 cm between the GNSS-based sea level measurements and tidal meter records). Li et al. [146] employed a combination of GNSS-R coastal wind data and ECMWF reanalysis products to enhance storm surge simulation. The results demonstrated improved accuracy, with a reduction in RMSE from 24.3 to 16.9 cm. This method represents a great progress in storm surge monitoring.

Future research can further explore and optimize the methods for detecting storm surges. When storm surge occurs, environmental factors such as waves, wind speed, and wave height on the ocean surface will have an impact on the reflected signals, and the data can be better understood and calibrated by modeling the relationship between the reflected signals and the environmental factors (e.g., waves, wind speed, etc.).

V. SEA ICE DETECTION, SEA ICE CONCENTRATION (SIC) RETRIEVAL, AND SEA ICE THICKNESS (SIT) RETRIEVAL USING SPACEBORNE GNSS-R

A. Sea Ice Detection

Sea ice is formed when seawater freezes in the ocean. It has a significant impact on the distribution of temperature and salinity on the ocean surface, as well as the density and circulation patterns of seawater. Sea ice also plays a role in regulating climate by reflecting solar radiation. Therefore, the detection and study of sea ice are crucial for understanding climate change, predicting changes in the marine environment, and protecting marine ecosystems. GNSS-R technology offers several advantages for sea ice detection and research. It allows for wide-ranging observations without the need for additional equipment, relying solely on existing navigation satellite systems and thus reducing costs. Furthermore, GNSS-R provides real-time monitoring data with high spatiotemporal resolution, making it one of the commonly used methods for detecting sea ice.

Komjathy et al. [147] were the first to propose the use of GNSS-R technology for sea ice detection with airborne instruments to receive GPS reflection signals. Wiehl et al. [148] simulated GPS ice sheet reflection and demonstrated the potential of GNSS reflection signals for ice sheet remote sensing. Rivas et al. [149] extracted dielectric constant and roughness data of ground scattering targets from reflected L-band GPS waveforms and used this information to infer the type of sea ice.

DDM is a crucial dataset for sea ice detection using GNSS-R as it contains rich information about sea ice conditions within sea areas. The primary difference between DDM of sea ice and seawater lies in diffusivity, allowing for classification of sea ice or seawater areas by evaluating DDM observables during sea ice detection.

Currently, sea ice detection methods are mainly divided into three categories: threshold-based methods, machine learning-based methods, and deep learning-based methods. Many researchers have extracted multiple observables from DDM (such as the DDW TES observable and DDW trailing edge waveform summation observable) and set optimal thresholds to distinguish between sea ice and seawater [150], [151], [152], [153], [154], [155]. However, relying solely on individual observables results in less than optimal accuracy in sea ice detection. In order to improve the accuracy of sea ice detection, machine learning methods (such as neural network (NN), decision tree (DT), random forest (RF), SVM, etc.) have been introduced for sea ice detection in [156], with the detection performance reaching over 95% in polar regions. Building upon this, in order to further improve detection performance by considering key feature information in DDM images, Yan and Huang [157] proposed a sea ice detection deep learning method based on CNN. The results show that the CNN-based method outperforms machine learning methods (such as NN), with a standard deviation error (Estd) ranging from 0.0016 to 0.0022.

Table VI summarizes and compares the methods of spaceborne GNSS-R sea ice detection mainly from the aspects of

TABLE VI
COMPARISON OF SPACEBORNE GNSS-R SEA ICE DETECTION METHODS

| Retrieve Models (Methods) | Literature | GNSS-R Data | Reference Data | GNSS-R Observations | Precision |
|------------------------------------|------------|----------------|---|---|---|
| NN | [158] | TDS-1 | Observation data of multiple sensors | DDM | The detection accuracy is about 98.4%, and the correlation coefficient is 0.93. |
| | [159] | FFSCat | OSI SAF sea ice extent maps | 12 observables (Averaged Delay Doppler Map (ADD), Elevation angle of the reflected signal and Reflectivity, etc.) | The OA for the sea ice extent maps is greater than 97% using microwave radiometry (MWR) data, and up to 99% when using combined GNSS-R and MWR data |
| CNN | [157] | TDS-1 | Observation data of Microwave Radiometer | DDM | The standard deviation error (Estd) is 0.0016 to 0.0022. |
| SVM and FS | [160] | TDS-1 | Observation data of passive microwave sensors | DDM | The detection accuracy is 98.56%. |
| DT and RF algorithms | [156] | TDS-1 | OSISAF SIE data | DDM-related variables and auxiliary variables | The sea ice monitoring methods based on RF and DT have detection accuracies of 98.03% and 97.51% in the Arctic region, and 95.96% and 95.46% in the Antarctic region, respectively. |
| Linear discriminant analysis (LDA) | [161] | TDS-1 | Surface type data of NOAA and data of SMOS | DDM | The detection accuracy is about 95.03%, and the correlation coefficient is 0.93. |
| Threshold analysis method | [155] | TDS-1 | Ground-truth data | DDM | The accuracy is as high as 99.73%. |
| | [152] | TDS-1 | AMSR2 data, OSISAF data | DDM | The probability of detecting sea ice is greater than 97%. |
| | [162] | FY-3E | OSI SAF SIC data | DDM | The OA of sea ice detection is 98.42%. |

retrieval methods, GNSS-R data, reference data, GNSS-R observations, and retrieval accuracy. It should be noted that only representative literature is listed in the table.

In GNSS-R-based sea ice detection, the accuracy is influenced by factors such as temperature and the mixture of sea ice and water. In the mixture of sea ice and water, due to the different physical properties of sea ice and water, the surface reflectivity and dielectric constant will change, which will affect the reflection of the GNSS-R signal. In the future, we should pay attention to these factors, and study relevant models and algorithms to improve the accuracy and reliability of sea ice detection.

B. Sea Ice Concentration and Sea Ice Thickness Retrieval

SIC and thickness are two crucial indicators for sea ice detection in the ocean. SIC refers to the extent of sea ice cover in a specific area of ocean surface, with 0% and 100% indicating open water and solid ice areas, respectively. Gleason [163] used spatial GPS detection signals reflected by sea ice to retrieve SIC and compared the results with those from advanced microwave scanners and sea ice maps. Semmling et al. [164], [165] studied the reflection power of GNSS observations and its sensitivity

to SIC based on ship-borne GNSS. Munoz-Martin et al. [166] presented some initial results of the PYCARO-2 instrument designed for the multidisciplinary drifting observatory MOSAiC for Arctic Climate Research, with a focus on the method of measuring ice and snow thickness using GNSS-R technology. Yan et al. [158] retrieved SIC and sea ice extent using NN and achieved high precision in detecting sea ice and estimating SIC, with an average accuracy of 98.4%. The method was validated with Nimbus-7 SMMR and DMSP SSM/I-SSMIS data, with an average absolute error of less than 9% and a correlation coefficient as high as 0.93. However, issues may arise with DDM collected near the ice edge of calm seas and low wind speeds that can lead to overestimated SIC and false positives. To evaluate the SIC estimate, the mean error E_{av} , the mean absolute error E_{abs} , the standard deviation error E_{std} , and the correlation coefficient R between SIC_{nn} and SIC_{ref} are employed for evaluation purposes and they are given by

$$\begin{cases} E_{av} = \text{mean}(SIC_{nn} - SIC_{ref}) \\ E_{abs} = \text{mean}(|SIC_{nn} - SIC_{ref}|) \\ E_{std} = \text{std}(SIC_{nn} - SIC_{ref}) \\ R = \frac{\text{cov}(SIC_{nn}, SIC_{ref})}{\text{std}(SIC_{nn})\text{std}(SIC_{ref})} \end{cases} \quad (10)$$

where E_{abs} is the mean absolute error, E_{std} is the standard deviation error, R is the correlation coefficient, SIC_{nn} is the NN-based SIC result, and SIC_{ref} is the reference SIC data of the day.

In recent years, researchers have made further progress in quantifying and analyzing the impact of low sea state on SIC estimation by utilizing more in situ sea state data and DDM data. Zhu et al. [167] utilized GNSS-R data from the TDS-1 satellite and analyzed the DDM to extract SIC information. They proposed a DDM-based observable called DDW and used the right edge waveform summation (REWS) of DDW to develop a retrieval model for SIC. Through validation with AMSR2 data, the RMSE of the retrieval SIC for the northern hemisphere and southern hemisphere is 11.78% and 12.10%, respectively.

Yang et al. [157], [168] developed an SIC retrieval method based on deep learning using GNSS-R DDM data. The RMSEs of the retrieval results in March and June 2016 were 0.0284 and 0.0415, respectively, which were compared with the SIC products of Hamburg University. The resulting SIC exhibited little deviation from the actual results, and the performance of the deep learning and NN-based methods was evaluated, proving that the deep learning-based GNSS-R retrieval SIC method has unique advantages over traditional methods.

SIT is also an important parameter to describe the state of sea ice and the state changes of sea ice (such as melting, deformation, and freezing) [3]. Because the sea ice state is greatly affected by environmental factors, the change process and existence state are complicated, so SIT retrieval is difficult. A traditional method commonly used is satellite altimeter measurements. Laxon et al. [169] collected satellite altimeter measurements of ice freeboard for eight years to retrieve and observe the SIT in the Arctic region. The thinning of Arctic sea ice is concluded. Giles et al. [170] used ENVISAT altimeter data to measure SIT in the Arctic region and found that the average SIT is decreased by 0.26 m. Microwave radiation measurement is another approach. Tian-Kunze et al. [171] proposed an SIT dataset based on soil moisture and ocean salinity (SMOS) to measure SIT. Huntemann et al. [172] developed a method to determine SIT by analyzing the high incidence angle of the SMOS satellite. By comparing thermodynamic ice growth data with SMOS brightness temperatures at incidence angles between 40° and 50°, they observed a high correlation with intensity and an inverse correlation with the difference between vertical and horizontal polarization brightness temperatures.

Spaceborne GNSS-R technology can provide detailed and accurate sea ice characteristics for monitoring SIT across the entire ocean area. With the advancement of machine learning, it has been applied to GNSS-R signal retrieval of SIT. Machine learning's powerful nonlinear fitting ability helps address the problem of multiple influencing factors caused by the complex environmental impact on sea ice conditions. Yan and Huang [173] compared the two machine learning-based SIT retrieval methods: CNN and support vector regression (SVR), the correlation coefficients were 0.95 and 0.90, respectively, and the root-mean-square (RMS) differences were 5.49 cm and 7.97 cm, respectively. This proves the capability of machine learning methods in retrieving SIT from GNSS-R data. Yan and Huang [174] analyzed the reflectance data of the TDS-1 satellite and

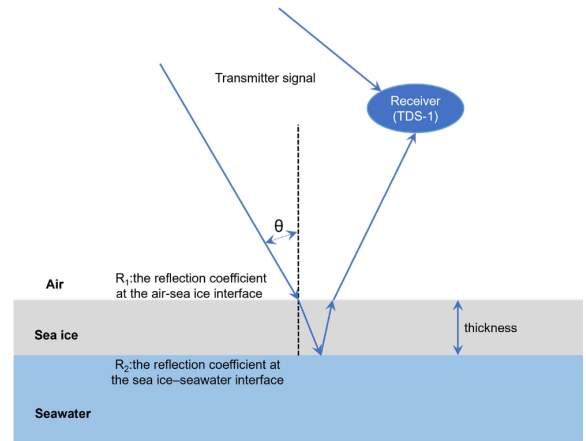


Fig. 3. Schematic diagram of GNSS-R signal reflecting from a three-layer model of air, sea ice, and seawater [174].

proposed a reflectance-based SIT estimation model [see (11)], which can be used to accurately estimate SIT). Fig. 3 shows the corresponding schematic diagram of GNSS-R signals reflected from the three-layer model of air, sea ice, and seawater. The model was validated using combined measurement results from SMOS and SMOS/SMAP as reference data. The derived TDS-1 SIT showed good agreement with the reference SIT, with a correlation coefficient (r) of 0.84 and an RMS difference of 9.39 cm when compared to SMOS, and a correlation coefficient of 0.67 and an RMSE of 9.49 cm when compared to SMOS/SMAP. This demonstrates the applicability of the developed model and the value of TDS-1 data in SIT estimation

$$d = \frac{-1}{4\alpha} \ln \frac{\Gamma}{|R_2|^2} \quad (11)$$

where α is the attenuation coefficient, Γ is the reflectivity, and R is the Fresnel reflection coefficient (the detailed derivation process of R is shown in [174]).

Munoz-Martin et al. [166] modeled the interference patterns generated by combining GNSS direct and reflected signals on the surface of sea ice and used a four-layer model to link the different thicknesses of the bottom layer (such as snow and ice) with the stripe positions of the interference patterns. Herbert et al. [175] inferred SIT from the FSSCat mission data using a predictive regression NN approach and illustrated preliminary results of the FSSCat mission in polar regions. Xie and Yan [176] utilized FY-3E data to conduct SIT retrieval employing a two-layer (sea ice-sea water) SIT retrieval model. The FY-3E dataset includes both GPS and BDS reflection signals. In comparison with the reference SIT, for the training set, the RMSE and correlation coefficient between GPS-R SIT and the reference were 0.1347 m and 0.8087, respectively, while for the test set, they were 0.1442 m and 0.7821, respectively. The results suggest that the BDS-based results exhibit a slight superiority over those obtained using GPS. Subsequently, Li et al. [177] employed an RF method to estimate SIT using FY-3E and SMOS data. Evaluation in the Arctic region demonstrated that the model trained on GPS and BDS signals from FY-3E achieved high consistency and low error. For GPS signals, coefficients of determination are 0.97 and

0.91, and mean absolute errors are 0.019 m and 0.032 m for the training and test sets, respectively.

Further investigations on thicker sea ice could be conducted in the future.

VI. RAINFALL DETECTION AND RAINFALL INTENSITY RETRIEVAL USING SPACEBORNE GNSSS-R

Rainfall is a critical factor in marine GNSS-R as it affects wind speed, SSH, and the retrieval of significant wave height. Therefore, detecting rainfall (RD) and measuring RI are essential aspects of marine remote sensing. To model the impact of raindrops on the water surface, researchers have used the first-order superposition concept, which incorporates the widely used rain-generated ring spectrum and the wind-induced Elfouhaily elevation spectrum. The ring spectrum is a logarithmic Gaussian model, which can be described as

$$S_K(K) = \frac{1}{2\pi} V_{Gr}(K) S_{Peak} \exp \left\{ -\pi \left[\frac{\ln \left(\frac{f(K)}{f_P} \right)}{\frac{\Delta f}{f_P}} \right]^2 \right\} \quad (12)$$

where $f(K)$ is given by the dispersion relationship $\sigma^2 = (2\pi f)^2 = gK + \frac{\tau}{\rho} K^3$; σ , g , K , ρ , and τ are radian frequency, gravitational acceleration ($\sim 980 \text{ cm}\cdot\text{s}^{-2}$), wave number, water density, and water surface tension ($\sim 74 \text{ cm}^3\cdot\text{s}^{-2}$), respectively; V_{Gr} is the group velocity at wavenumber K , and S_{Peak} is the power-law spectral model given by $6 \times 10^{-4} R^{0.53} \text{ cm}^2\cdot\text{Hz}^{-1}$; $f_P = 5.772 - 0.0018R$ Hz. Bliven et al. [178] estimated the model coefficients to represent circular waves in the frequency range of 2.75–12 Hz (wavelengths 1.94–20.8 cm).

Various RD methods based on X-band radar have been proposed by researchers [179], [180], [181]. Lund et al. [179] utilized the zero-pixel percentage (ZPP) method, which considers the impact of rainwater on the intensity of zero pixels as a quality control factor for rainfall presence, thus improving the accuracy of wind speed retrieval. To further enhance the accuracy of RD, Lu et al. [182] introduced the ratio of zero-intensity to echo method based on the ZPP method. Experimental results indicated an 11.4% improvement in accuracy compared to ZPP. Chen et al. [180] proposed an RD method based on SVM and compared it with the ZPP method, demonstrating higher accuracy with the SVM-based approach. Zheng et al. [181] discovered a certain correlation between the spatiotemporal characteristics of sea clutter and the correlation coefficient of rainy versus nonrainy wave images, and based on this, they proposed a new RD method.

RI reflects the magnitude of rainfall, which has significant implications for the marine environment and navigational safety. In addition, in the context of wind-wave information retrieval, RI also indicates its impact on the accuracy of wind-wave retrieval results [181], [182]. To improve the reliability of wind-wave retrieval results, it is advisable to discard data with relatively high RI values.

Traditional methods for RI estimation involve using rain gauges, which provide accurate results due to direct measurement of RI. However, they have limitations in terms of measuring RI within a small range and having poor spatial-temporal

distribution characteristics [183], [184]. Ground-based radar measurements are also commonly used for RI retrieval but they are often affected by issues such as signal attenuation and reflectivity problems [185]. Remote sensing methods have made significant progress in large-scale RI retrieval [186], [187], [188]. Tian et al. [189] proposed two models based on BPNN and CNN and compared them with traditional meteorological service system methods. Results from all three methods showed that deep learning algorithms outperformed traditional methods, with a reduction in mean square error by 75.84% and 82.30%, respectively.

In addition to traditional methods, the development of meteorological satellites has led to the availability of various open-source rainfall products that are widely used in hydrology, meteorology, environmental science, and other fields. Some of these products include Climate Prediction Center MORPHing (CMORPH), Tropical Rainfall Measurement Mission (TRMM) Multi-satellite Precipitation Analysis (TMPA), Precipitation Estimation from Remotely Sensed Information using ANNs (PERSIANN), Integrated Multi-satellite Retrievals for GPM (IMERG), TRMM3B42v7, Global Satellite Mapping of Precipitation (GSMAP), Climate Hazards Group Infrared Precipitation with Stations (CHIRPS), ERA5, ECMWF Reanalysis Interim (ERA Interim), and SM2Rain-ASCAT (Advanced Scatterometer) rainfall products. Among these, IMERG has been found to exhibit the best performance in rainfall estimation [190], [191], [192].

GNSS-R, as a new remote sensing method, has achieved certain accomplishments in the field of oceanography, as mentioned earlier. However, research on RD using GNSS-R is limited. Asgarimehr et al. [193] were the first to extract rainfall characteristics from GNSS-R data collected by TDS-1. Balasubramaniam and Ruf [194] also analyzed the impact of rainfall on GNSS-R ocean measurements, noting that GNSS-R in the L-band is more capable of penetrating rain and cloud layers compared to scatterometers. However, intense rainfall can cause changes in sea surface roughness that affect the measurements [178]. Bu and Yu [195] conducted preliminary research on RD and RI retrieval using spaceborne GNSS-R technology. They proposed a GNSS-R observable threshold RD method based on probability density functions (PDFs). Unfortunately, the PDF method did not consider several important parameters, which limited the accuracy of RD. Subsequently, Bu and Yu [120] used CYGNSS DDM data to study RD over the ocean and proposed three new methods for spaceborne GNSS-R RD: SVM, RF, and CNN. The research results indicated that the SVM and RF methods have similar RD accuracy, while the CNN method outperformed the other two methods, achieving an improvement of over 10% compared to the PDF method.

Previous studies have confirmed the ability of GNSS-R technology to detect rainfall over the ocean. However, there is a need for further research on RI retrieval. Bu et al. [196] developed three models for spaceborne GNSS-R retrieval of RI over the ocean: DDMA, LES-NIDW, LEWS-NIDW, and REWS-NIDW. They extensively evaluated the RI retrieval results obtained from the three models against reference data (IMERG-F). This research demonstrated the significant potential of spaceborne

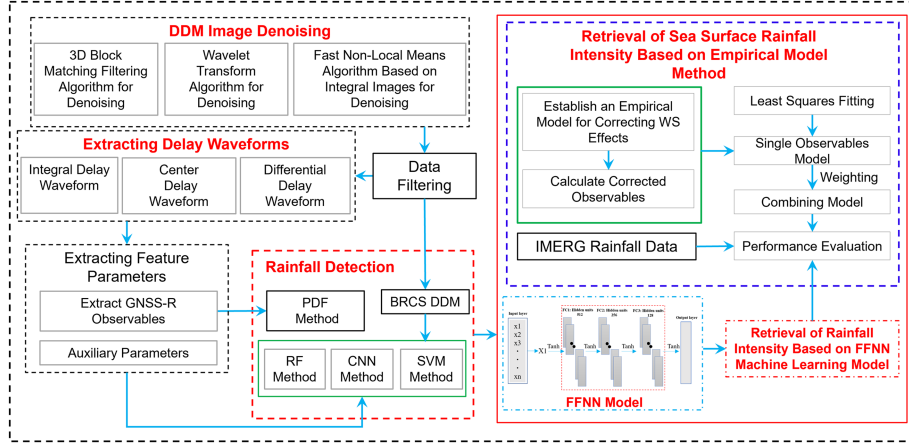


Fig. 4. Method and process of RD and RI retrieval for spaceborne GNSS-R [115], [195], [196], [197].

GNSS-R for RI retrieval over the ocean. Fig. 4 summarizes the general methods and technical processes for RD and RI retrieval using spaceborne GNSS-R up to the present time. In 2023, Bu et al. [115] conducted a study on joint retrieval of sea surface wind speed, RI, and wave height using spaceborne GNSS-R data. The research emphasized the necessity of estimating and correcting rainfall interference in wind and wave height measurements and highlighted the importance of using spaceborne GNSS-R technology for RD and RI estimation to improve the accuracy of wind and wave retrieval. In addition, sea surface wind and waves significantly influence rainfall over the ocean and serve as major interfering factors in rainfall monitoring. Therefore, future research should focus on investigating the impact of sea surface wind and waves, especially under complex sea conditions, on rainfall monitoring using spaceborne GNSS-R.

VII. OTHER NEW APPLICATIONS

A. Ionospheric Monitoring Using Spaceborne GNSS-R

The ionosphere is a region of the upper atmosphere consisting of free electrons and ions resulting from the ionization of molecules and atoms by solar radiation. It plays a critical role in space weather studies, satellite operations, and remote sensing observations [198]. Ionospheric monitoring primarily involves measuring electron density (ED), total electron content (TEC), and ionospheric weather. ED and TEC are the main measurement tasks.

Voxel tomography is a traditional method for ionospheric monitoring, but it involves a large number of unknowns. Therefore, some researchers, such as Pallares et al. [199] have used hydrogen atomic imaging to derive ED from ionospheric TEC.

In recent years, significant progress has been made in TEC monitoring using GNSS. However, due to the relatively sparse distribution of receivers in marine and remote areas, measurement errors may occur [200], [201], [202].

To solve this problem, some researchers have studied the use of GNSS reflected signals from the ocean to measure ionosphere-related parameters. Zhang et al. [198] studied the effect of ionospheric delay on SSH measurement, eliminated

this effect through spatial filtering, and determined the optimal filtering parameter values. Molina and Camps [203] used GNSS-R data from the CYGNSS mission to explore new sources of data on plasma loss (EPBs). Evidence for the first detection of ionospheric bubbles in ocean areas using GNSS-R data, and their size, duration, and increased intensity of flickers can be measured ($S4$). The study found that the detected bubbles had an $S4$ value of about 0.3–0.4 and lasted from a few seconds to a few minutes. Liu et al. [204] proposed a new algorithm that integrated slant TEC (sTEC) measurements from GNSS-R CubeSats and ground GNSS receivers to generate a map of vertical TEC in the Arctic. The results demonstrated that this method captured high spatial and temporal resolution, as well as high-precision features of the ionospheric structure in high latitudes. Ren et al. [202] used CYGNSS to monitor the ionosphere, improving the detection of ionospheric irregularity. The ionospheric regularity index $S4_R$ was derived and verified using the SNR measurement data from GNSS-R [SNR measurement was used to estimate the equivalent $S4_R$ value, as shown in formula (13)]. The CYGNSS-derived $S4_R$ was evaluated and analyzed along with the ionospheric irregularity data from ground-based (GNSS and Ionospheric Sounder) and spaceborne (Swarm and FORMOSAT-3/COSMIC) instruments

$$\begin{cases} I_{\text{SNR}} = 10^{\frac{\text{SNR}_{\text{DDM}}}{10}} \\ S4_R = \sqrt{\frac{\langle I_{\text{SNR}}^2 \rangle - \langle I_{\text{SNR}} \rangle^2}{\langle I_{\text{SNR}} \rangle^2}} \end{cases} \quad (13)$$

where $\langle I_{\text{SNR}} \rangle$ denotes the average value. The value of the SNR is given in decibels (dB).

In addition, they proposed an improved method that takes into account the influence of ionospheric and tropospheric delays above the GNSS-R receiver, and uses the LS fitting method to achieve the best match between measured and simulated DDM. The LS fitting process for measuring and simulating DDM is shown in [201]. To assess the performance of their method, they compared it with two ionospheric empirical models (NeQuick2 and IRI-2016), the GIM final product, and the measured GNSS TEC. The assessments were conducted for

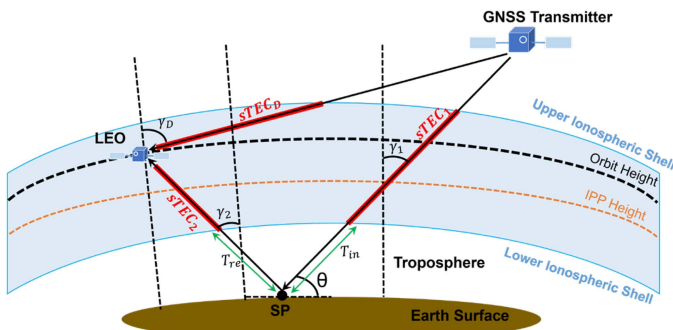


Fig. 5. Diagram of sTEC along the direct line of sight and reflected GNSS signal received at LEOs [205].

two periods, May 2015 and May 2017, under different solar activity conditions. The results show that the proposed method improves the RMS during high and low solar activity by 5.3% and 23.5%, respectively. This improvement is significant for modeling the ionosphere over ocean areas [201]. Wang and Morton [200] used coherent GNSS-R measurements from LEO CubeSats to observe ionospheric TEC and plasma structure, and the results showed that GNSS-R has the potential to fill the gap in ionospheric observation data in polar regions and improve global ionospheric TEC observations over oceans and inland waters. Fig. 5 shows the schematic diagram of the sTEC and LEO receiving reflected GNSS signals. In the figure, γ represents the elevation angle of the incident ray at the ionospheric pierce point, sTEC represents the slant total electron content, subscripts 1, 2, and D represent the incident ray, reflected ray, and direct path of the ionosphere, respectively, and θ represents the elevation angle at the SP. T_{in} and T_{re} correspond to the ionospheric errors in incident ray and reflected ray.

Currently, GNSS-R measurements using LEO CubeSats to observe the ionospheric TEC and plasma structure present some challenges (e.g., differential code bias (DCB) estimation errors in receivers and carrier phase skip correction in coherent GNSS-R signal processing). Therefore, future research should focus on characterizing the relationship between DCB and elevation and azimuth and designing internal DCB calibration systems.

B. Sea Surface Salinity (SSS) Measurement Using Spaceborne GNSS-R

SSS refers to the concentration of salt in the surface waters of the ocean, and it is a vital parameter for studying seawater's salt content. Collecting data on ocean salinity is crucial for understanding global ocean circulation and climate change. In this regard, satellite sensors play a key role as they can monitor SSS in real time and provide accurate data for scientific research. Through observations from satellite sensors, we can gain a comprehensive understanding of the spatial distribution and temporal variations of ocean salinity, which are essential for marine environmental protection, resource management, and climate forecasting.

Satellites used for monitoring SSS include the ESA's SMOS mission. Launched in 2009, the SMOS satellite detects SSS using L-band brightness temperature (TB) measurements [206].

Prior to its launch, researchers extensively discussed the planning [207], development [208], and error estimation [209], [210] of the SMOS salinity retrieval mission. They also studied the feasibility and accuracy requirements for SSS retrieval [211]. The launch of the SMOS satellite significantly contributed to the research on SSS retrieval. However, the lack of reliable and colocated auxiliary fields in SMOS retrieval has limited its scientific application. Encouragingly, some researchers conducted preliminary studies on the potential application of GNSS-R signals for ocean salinity retrieval [212], [213]. Subsequently, other researchers improved the feasibility of SSS retrieval by combining measurements from L-band radiometers and GNSS-R [214]. While L-band radiometry is a commonly used technique for measuring SSS from spaceborne observations, Kainulainen et al. [215] observed a new correlation between sea surface roughness information collected by GNSS-R and radiometric measurements from L-band radiometer systems. They validated the capability of the HUT-2-D aperture synthesis radiometer to detect variations in ocean salinity.

The Aquarius/SAC-D mission, launched in 2011, is a collaboration between NASA and the Argentine Space Agency (CONAE). Its main instrument, the Aquarius Salinity Scanning Radiometer, is used to measure the salinity of oceans. Le Vine et al. [216] explained how Aquarius, along with remote sensing techniques, can monitor seasonal and interannual variations in SSS. This helps improve our understanding of ocean circulation, global water cycling, and climate. Valencia et al. [217] demonstrated the potential of using L-band microwave radiometers for calibration in future salinity missions through ALBATROSS field experiments.

In 2015, NASA launched the SMAP mission, which was primarily designed to measure soil moisture and landscape freeze-thaw, but also utilized L-band radiometry to measure SSS [218]. Fore et al. [219] developed and validated measurement algorithms for ocean vector winds and SSS estimation using SMAP's combined active/passive measurements. However, obtaining SSS from spaceborne L-band radiometers has always been a challenging task.

In 2019, Sharma [220] proposed a new method for determining SSS from SMAP and verified the potential capability of this retrieval technique in capturing SSS changes on a daily and monthly basis. Dinnat et al. [218] compared the differences between the ocean surface salinity results obtained by three satellite remote sensing sensors (SMOS, Aquarius, and SMAP) and the in-situ observation data. They also analyzed the influence of retrieval parameters on these differences.

SMOS, Aquarius, and SMAP all retrieve SSS using iterative algorithms, which are usually based on the statistical relationship between observed data and the model parameters, using multiple observational features such as TB and polarizability, to estimate SSS. The iterative algorithm that minimizes an estimator, or cost function, has the following general expression [218]:

$$\ell^2 = \sum_{\theta, \text{pol}} \frac{(TB_{\text{obs}} - TB_{\text{mod}})^2}{\sigma_T^2} + \sum \frac{(M_{\text{trr}} - M_{\text{anc}})^2}{\sigma_{\text{pol}}^2} \quad (14)$$

where θ is the sum of squared differences in TB combines multi-incidence angles, pol represents multiple polarizations, TB_{obs} is the observed TB, TB_{mod} is the TB calculated using the radiative transfer model, σ_T^2 is the estimated variance of TB, M_{rr} is the retrieved auxiliary parameter, and M_{anc} is the auxiliary data.

In 2021, the ESA launched the Federated Satellite System (FSSCat) mission, which utilized data from the Flexible Microwave Payload-2 (FMPL-2) to estimate soil moisture and SIC at a coarse resolution. In addition, FMPL-2 data were used to estimate SSS [221]. Liu et al. [222], [223] integrated CYGNSS data into the SSS retrieval algorithm of the SMAP mission to enhance salinity detection accuracy, particularly under low wind speed conditions. They also examined the sensitivity of SMOS and SMAP brightness temperatures to CYGNSS data for investigating the potential of using spaceborne GNSS-R to improve the precision of SSS measurements.

In recent years, research efforts have been directed toward enhancing the accuracy of SSS retrieval. These studies have primarily focused on improving remote sensing techniques [220] and optimizing algorithm models [224], aimed at providing a more solid data foundation for climate research and marine science. Many researchers have utilized machine learning methods to improve spaceborne SSS retrieval. Rajabi-Kiasari and Hasanlou [225] deployed machine learning-based methods to correct SSS products retrieved by L-band microwave sensors. Four machine learning methods, namely SVR, ANN, RF, and gradient boosting machine (GBM), were employed to model SSS, among which GBM produced slightly better results (with an RMSE of 0.906). Jang et al. [226] used three machine learning methods (i.e., RF, ANN, and SVR) to improve SMAP SSS retrieval. All three machine learning models outperformed SMAP SSS, with RF exhibiting the best performance and generating the lowest RMSE (0.203 and 0.556 psu). In another study, Jang et al. [227] proposed a new global SSS model based on seven machine learning methods, including K-nearest neighbor, SVR, ANN, RF, extreme gradient boosting, light gradient boosting models, and gradient boosted regression trees (GBRT). The global SSS model based on GBRT yielded the best results with a coefficient of determination (R^2) of 0.99 and a root mean square deviation (RMSD) of 0.259 psu. The retrieval of SSS is highly dependent on correcting sea surface TB. Li et al. [228] preliminarily verified the correlation between CYGNSS observables and TB variations. They discovered that incidence angles need to be considered when acquiring SSS with SMAP and CYGNSS. To evaluate the detection performance of SMAP and SSS with different parameter combinations, a multilayer perceptron (MLP) model is developed. The results show that the retrieval performance based on the MLP model is superior to that based on the GMF model.

In the future, deep learning methods hold great potential for improving the accuracy of sea salinity retrieval. With their powerful pattern recognition and feature extraction capabilities, deep learning algorithms can learn complex nonlinear relationships from ocean observation data. This enables them to provide more accurate predictions and simulations of SSS. Leveraging deep learning, large-scale observational and simulation datasets can be useful for training to further optimize the performance of SSS

models. Overall, the application of deep learning in SSS retrieval has significant potential for advancing the field and improving our understanding of the ocean environment.

C. Monitoring Phytoplankton Using Spaceborne GNSS-R

Phytoplankton refers to a category of small plants found in the ocean, including various types of microalgae and bacteria. They are diverse in species and widely distributed. The abundant proliferation of phytoplankton is often triggered by an excess of nutrients in the ocean. These nutrients, combined with sunlight, promote the growth and reproduction of phytoplankton, resulting in a thin layer on the ocean surface and reducing surface roughness. Human activities in the ocean exacerbate the harm to marine environments and ecosystems in some sense. Eutrophication of seawater can lead to phenomena such as algal blooms and red tides, which are marine ecological events characterized by rapid phytoplankton proliferation in highly eutrophic areas.

In the past, remote sensing techniques such as optical remote sensing, thermal infrared remote sensing [229], [230], and microwave remote sensing [231] were commonly used to monitor harmful algal blooms.

In recent years, the development of GNSS-R has rapidly advanced, providing a new observational method for monitoring phytoplankton. Rodriguez-Alvarez and Oudrhiri [232] were the first to use the dust deposition of the 2020 Sahara sandstorm as a background to verify that GNSS-R is an effective tool for mapping the phytoplankton coverage. They also demonstrated the ability of CYGNSS data to detect and monitor phytoplankton proliferation.

The frequent outbreaks of red tide have had significant negative impacts on the marine environment and ecosystem. The occurrence and development of red tide can cause fluctuations in sea surface temperature (SST). When monitoring red tide, it is often challenging to obtain SST directly through remote sensing technology. Therefore, a commonly used method is to select brightness temperature as a proxy for SST and monitor the physical characteristics of the sea surface [217]. The expression for TB is as follows [209]:

$$T_B(\theta) = T_{B,\text{flat}}(\theta, f, \text{SSS}, \text{SST}) + \Delta T_B(\theta, p) \quad (15)$$

where θ is the signal incidence angle, f is the carrier frequency of GNSS signal, p is the surface roughness, SSS is the salinity of the sea surface, $T_{B,\text{flat}}$ is the brightness temperature of the flat sea surface, and ΔT_B is the brightness temperature change caused by the fluctuation of the sea surface state.

Ban et al. [233] combined GNSS-R technology with the changes in the sea surface caused by red tide growth and established the relationship between GNSS-R observations and environmental factors influencing red tide, enabling the monitoring and early warning of red tides. However, unlike red tides, green tide algae tend to aggregate and have low satellite resolution, which may not be the optimal method for monitoring green algae. Ban et al. [234] proposed a novel method to retrieve green algae density from GEO satellite reflection signals collected by a shipborne receiver. This method validated that GEO-R signals can achieve continuous monitoring of green algae in the same

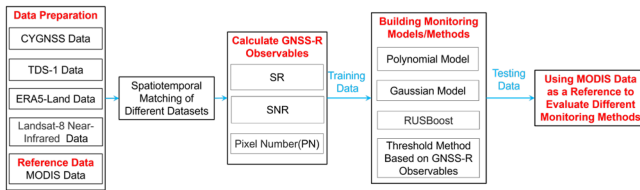


Fig. 6. Technological process of Spaceborne GNSS-R phytoplankton monitoring [232], [233], [236].

area, better adapting to the floating and moving characteristics of green algae.

Furthermore, Ban et al. [235] proposed a new method to monitor green algae density using ground-based GNSS-R observations. Their method utilizes the relationship between seawater dielectric constant and changes in sea surface conditions caused by green algae to detect green algae density through variations in sea surface TB. Both of these methods address the issues of existing green algae remote sensing via optical sensors, which are heavily influenced by weather conditions and have long revisit times.

Recently, Zhen and Yan [236] developed a method based on machine learning and auxiliary meteorological data to improve Spaceborne GNSS-R monitoring of algal blooms. Their results showed significant improvements in detection accuracy with the inclusion of meteorological data. The true positive rate was 81.9%, the true negative rate was 82.9%, and the overall accuracy (OA) was 82.9%. The area under the curve was found to be 0.88. The technical route of spaceborne GNSS-R phytoplankton monitoring is depicted in Fig. 6.

In the future, more improvements need to be made in the monitoring accuracy of phytoplankton, which can further be improved by applying other ML methods.

D. Sea Surface Target Detection Using Spaceborne GNSS-R

Sea surface target detection is an important research direction in the field of remote sensing, with significant implications for maritime traffic monitoring, vessel search and rescue, and environmental monitoring. In recent years, GNSS-R has shown great potential as an emerging remote sensing method in the field of sea surface target detection. Compared to traditional active radar or optical remote sensing techniques, GNSS-R offers unique advantages such as weather independence, low power consumption, all-weather availability, and low cost. These characteristics have made GNSS-R one of the highly regarded research directions in sea surface target detection.

Significant progress has been made in the research on sea surface target detection using GNSS-R. Valencia et al. [237], [238] proposed a GNSS-R-based method for retrieving sea surface scattering coefficients, which can effectively detect oil slicks on the ocean surface. Valencia et al. [239] further explored the method for detecting oil films on the ocean surface using GNSS-R data. Ji et al. [240] discussed a method for detecting and locating marine targets based on spatial GNSS-R DDM. Similarly, Simone et al. [241] conducted a similar study

successfully distinguishing the reflection characteristics of target objects from background clutter.

In the process of distinguishing between sea clutter and sea surface targets, estimation of sea clutter is carried out, and it is subtracted from the DDM to highlight the characteristics of sea targets. However, in spaceborne GNSS-R measurements, Doppler tracking errors may occur due to factors such as signal propagation delay, motion of the reflecting surface, and dynamics of the receiving platform, making target detection not always reliable. To address these challenges, Cheong et al. [242] proposed two blind methods for suppressing sea clutter: adaptive filters and infinite pulse response low-pass filters. Experimental results show that both proposed methods can significantly detect potential maritime targets. Furthermore, the adaptive filters have qualitative features that make the DDM features of maritime targets more prominent than other maritime suppression methods. Southwell et al. [243] proposed a spatial GNSS-R ocean target detection method based on matched filters and compared it with other methods, demonstrating its effectiveness and superiority in detecting sea targets. Liu et al. [244] introduced a GNSS-R multiobject detection and localization method based on consistency check. Their method combines time-domain and frequency-domain information to improve detection performance. Li et al. [245] estimated offshore clutter and eliminated positional ambiguity by fusing data from multiple GNSS-R satellites, thereby achieving the detection and positioning of offshore oil wells.

Currently, there are numerous studies on the use of GNSS-R for sea surface target detection, particularly for ship detection. Simone et al. [246] proposed a novel method for detecting ships by analyzing the characteristics of reflected signals. The method utilizes specific signal features formed by echo scattering and utilizes adaptive filtering and correlation analysis to improve detection performance. In addition, Simone et al. [247] evaluated the feasibility of ship detection in spaceborne GNSS-R data through comparative analysis and analyzed the traditional GNSS-R technology from two aspects: acquisition geometry and receiving polarization channel. Subsequently, Simone et al. [248] verified the feasibility and effectiveness of using GNSS-R DDM in ship detection through simulation experiments and discussed the influence of acquisition geometry conditions and polarization modes on ship detection performance. The study provides a feasible scheme for the application of GNSS-R in the field of sea target detection. Beltramonte et al. [249] also verified the feasibility of using GNSS-R DDM for ship detection through simulation experiments, discussed the influence of parameters on detection performance, and proposed some improvement methods. Furthermore, Zhao et al. [250] proposed a new method that combines aerospace SAR and GNSS-R technology for ship detection. By analyzing the characteristic information of SAR images and GNSS-R DDM and combining them, the accuracy and robustness of target detection can be improved.

GNSS-R is a promising tool for sea surface target detection and monitoring, and future research should focus on improving the accuracy and reliability of GNSS-R data, optimizing the acquisition geometry and polarization settings, and developing new sea surface target detection and monitoring algorithms.

E. Sea Surface Microplastics Detection Using Spaceborne GNSS-R

Sea surface microplastics refer to small particles or fibrous plastic particles distributed on the ocean surface. The size of sea surface microplastics is generally below 5 mm and can even reach the nanometer level. Addressing the issue of sea surface microplastics requires global action. Therefore, conducting global-scale detection of sea surface microplastics is highly necessary. It can help us understand the temporal and spatial distribution of sea surface microplastics, enabling better responses to the issue and safeguarding the health and sustainable development of marine ecosystems.

Radar measurements are employed to estimate the concentration of microplastics in the ocean. Such a method entails examining the deviation between the measured ocean roughness and that predicted by a model based on surface wind speed. According to the research conducted by Evans and Ruf [251], roughness can be characterized by the mean square slope (MSS) of surface height, and there exists a robust correlation between MSS anomalies and simulated microplastic concentrations. Standardized MSS exception is defined as

$$\text{MSS}_{\text{anom}} = \frac{\text{MSS}_{\text{obs}} - \text{MSS}_{\text{mod}}}{\text{MSS}_{\text{mod}}} \quad (16)$$

where MSS_{obs} is the MSS measured by CYGNSS, and MSS_{mod} is the model predicted MSS

$$\text{MSS}_{\text{mod}} = \begin{cases} 0.0035(U + 0.62), & \text{if } U \leq 3.49 \text{ m/s} \\ 0.0035(6 \ln(U) - 3.39), & \text{if } U > 3.49 \text{ m/s} \end{cases} \quad (17)$$

where U is the ocean surface wind speed.

In recent years, GNSS-R has gained significant attention in the field of ocean remote sensing. The pollution caused by marine microplastics has emerged as a crucial environmental issue worldwide. To tackle this problem, researchers have started exploring the potential of GNSS-R technology for detecting and imaging microplastics in the ocean.

Gonga et al. [252] conducted an experimental study focusing on the detection of marine microplastics. They created a simulated ocean environment in a tank and performed experiments using the reflection signals observed through GNSS-R. By analyzing the characteristics of the reflected signals, they successfully detected microplastics in simulated seawater and conducted quantitative analysis. The research findings suggest that GNSS-R technology holds promise for monitoring marine microplastics. However, it is important to note that the research on using GNSS-R technology for microplastic detection is still in its early stages, requiring further experimental verification and algorithm refinement.

Future research endeavors can focus on developing more accurate and efficient GNSS-R data processing algorithms. In addition, designing advanced instruments and equipment and integrating other remote sensing technologies for multisource data fusion can enhance the accuracy and feasibility of marine microplastic detection.

VIII. SUMMARY AND FUTURE PROSPECTS

The article provides a comprehensive overview of recent advancements in the application of GNSS-R technology in marine remote sensing. It covers various innovative applications such as sea surface wind speed and direction; hurricanes, typhoons, and tropical cyclones; tsunamis and storm surges; SSH and wave height (e.g., SWH, Swell height), sea ice; rainfall, and ionosphere and SSS.

In addition to the aforementioned hot research topics on spaceborne GNSS-R, there are several other valuable scientific research areas that have gained widespread attention. For instance, Hoseini et al. [253] pioneered the use of spaceborne GNSS-R technology to detect mesoscale ocean eddies. They demonstrated the feasibility of using NBRCS to identify the center or edge of these eddies. This study holds great significance in advancing the detection of mesoscale ocean eddies through spaceborne GNSS-R. Hoseini and Nahavandchi [254] analyzed the detectability of sea surface currents using spaceborne GNSS-R data and compared it with wind and near-surface ocean current measurements. They confirmed the impact of sea surface currents on spaceborne GNSS-R NBRCS observations. While their study primarily focused on the combined effect of wind and ocean currents on GNSS-R, it is important to consider other factors such as swell, surfactants, and precipitation that may influence GNSS-R observations in future research. The spaceborne GNSS-R carrier phase measurement method was proposed in [255] and [256] to estimate sea ice height. The measurement values of ICESat-2 (or mean sea surface model) were compared with GNSS-R retrieval results showing good consistency. Although the main source of error in sea ice height retrieval is caused by the delay in the troposphere, these studies demonstrate the potential of using coherent carrier phase observations to achieve centimeter-level ice height measurement accuracy. However, future research in spaceborne GNSS-R sea ice height should prioritize tropospheric delay correction to enhance retrieval accuracy.

Recently, Buendía et al. [257] utilized GA GNSS-R to retrieve sea ice height and validated the results using digital elevation models. Their findings confirmed the feasibility of using GA GNSS-R for measuring sea ice height. Notably, in 2023, Wang [258], [259] was the first to use GA GNSS-R to measure tropospheric delay and water vapor content. He estimated tropospheric delay using dual-frequency GPS signals collected by GA from sea ice reflection, and compared them with ERA5 products. The results showed that the GNSS-R method had good consistency with ERA5. The study broadens the application scope of GNSS-R in the field of ocean remote sensing.

Although spaceborne GNSS-R has made significant progress in marine remote sensing in recent years and introduced many new concepts and methods, the technology is not yet mature. One challenge lies in the limited generality of the developed empirical and semiempirical models, which restrict their applicability to specific scenarios. In addition, machine learning and deep learning models often lack strong generalization capabilities and can be prone to underestimation or overestimation due to imbalanced training data distribution. Therefore, there is a

pressing need to enhance the robustness and generality of these models to facilitate their widespread application.

As an emerging remote sensing technology, it is necessary to develop advanced spaceborne GNSS-R modeling algorithms suitable for different applications, producing new products with performance comparable to traditional remote sensing techniques or combining with other technologies to achieve improved products. In addition, conducting ground-based and airborne experiments for new GNSS-R applications is crucial to refine the fundamental theories/models (electromagnetic scattering models for L-band signals) and further develop spaceborne GNSS-R. To further enhance the capabilities of spaceborne GNSS-R, it is essential to optimize the design of next-generation instruments and perform in-orbit experiments to enable multi-frequency/multisystem, multipolarization, and multiobservation mode capabilities. Expanding the application fields and scenarios of spaceborne GNSS-R to retrieve additional geophysical parameters and detect other natural events or phenomena is also a pressing goal for the future. This will contribute to the continued growth and utilization of spaceborne GNSS-R in a wide range of remote sensing applications.

ACKNOWLEDGMENT

The authors would like to thank the anonymous reviewers for their in-depth reviews and helpful suggestions that have largely contributed to improving this article.

REFERENCES

- [1] S. Jin, G. P. Feng, and S. Gleason, "Remote sensing using GNSS signals: Current status and future directions," *Adv. Space Res.*, vol. 47, no. 10, pp. 1645–1653, 2011.
- [2] N. Rodriguez-Alvarez, J. F. Munoz-Martin, and M. Morris, "Latest advances in the global navigation satellite system—Reflectometry (GNSS-R) field," *Remote Sens.*, vol. 15, no. 8, 2023, Art. no. 2157.
- [3] K. Yu et al., "Spaceborne GNSS reflectometry," *Remote Sens.*, vol. 14, no. 7, 2022, Art. no. 1605.
- [4] H. Carreno-Luengo et al., "The IEEE-SA working group on spaceborne GNSS-R: Scene study," *IEEE Access*, vol. 9, pp. 89906–89933, 2021.
- [5] C. D. Hall and R. A. Cordey, "Multistatic scatterometry," in *Proc. Int. Geosci. Remote Sens. Symp., 'Remote Sens.: Moving Toward 21st Century'*, 1988, vol. 1, pp. 561–562.
- [6] M. Martin-Neira, "A passive reflectometry and interferometry system (PARIS): Application to ocean altimetry," *ESA J.*, vol. 17, pp. 331–355, 1993.
- [7] J. Garrison, S. Katzberg, and M. Hill, "Effect of sea roughness on bistatically scattered range coded signals from the global positioning system," *Geophys. Res. Lett.*, vol. 25, pp. 2257–2260, 1998.
- [8] V. U. Zavorotny and A. G. Voronovich, "Scattering of GPS signals from the ocean with wind remote sensing application," *IEEE Trans. Geosci. Remote Sens.*, vol. 38, no. 2, pp. 951–964, Mar. 2000.
- [9] S. T. Lowe, J. L. LaBrecque, C. Zuffada, L. J. Romans, L. E. Young, and G. A. Hajj, "First spaceborne observation of an Earth-reflected GPS signal," *Radio Sci.*, vol. 37, no. 1, pp. 1–28, 2002.
- [10] S. Gleason et al., "Detection and processing of bistatically reflected GPS signals from low Earth orbit for the purpose of ocean remote sensing," *IEEE Trans. Geosci. Remote Sens.*, vol. 43, no. 6, pp. 1229–1241, Jun. 2005.
- [11] M. P. Clarizia, C. S. Ruf, P. Jales, and C. Gommenginger, "Spaceborne GNSS-R minimum variance wind speed estimator," *IEEE Trans. Geosci. Remote Sens.*, vol. 52, no. 11, pp. 6829–6843, Nov. 2014.
- [12] G. Foti et al., "Spaceborne GNSS reflectometry for ocean winds: First results from the U.K. TechDemoSat-1 mission," *Geophys. Res. Lett.*, vol. 42, no. 13, pp. 5435–5441, Jul. 2015.
- [13] C. S. Ruf et al., "New ocean winds satellite mission to probe hurricanes and tropical convection," *Bull. Amer. Meteorological Soc.*, vol. 97, no. 3, pp. 385–395, 2016.
- [14] C. Jing, X. Niu, C. Duan, F. Lu, G. Di, and X. Yang, "Sea surface wind speed retrieval from the first Chinese GNSS-R mission: Technique and preliminary results," *Remote Sens.*, vol. 11, no. 24, 2019, Art. no. 3013.
- [15] G. Yang et al., "FY3E GNOS II GNSS reflectometry: Mission review and first results," *Remote Sens.*, vol. 14, no. 4, 2022, Art. no. 988.
- [16] J. Wickert et al., "GEROS-ISS: GNSS reflectometry, radio occultation, and scatterometry onboard the international space station," *IEEE J. Sel. Topics Appl. Earth Observ. Remote Sens.*, vol. 9, no. 10, pp. 4552–4581, Oct. 2016.
- [17] Q. Yan and W. Huang, "Sea ice remote sensing using GNSS-R: A review," *Remote Sens.*, vol. 11, no. 21, 2019, Art. no. 2565.
- [18] M. P. Clarizia, C. Gommenginger, S. Gleason, C. Galdi, and M. Unwin, "Global navigation satellite system-reflectometry (GNSS-R) from the U.K.-DMC satellite for remote sensing of the ocean surface," in *Proc. IEEE Int. Geosci. Remote Sens. Symp.*, 2008, pp. I-276–I-279.
- [19] M. Unwin, P. Jales, J. Tye, C. Gommenginger, G. Foti, and J. Rosello, "Spaceborne GNSS-reflectometry on TechDemoSat-1: Early mission operations and exploitation," *IEEE J. Sel. Topics Appl. Earth Observ. Remote Sens.*, vol. 9, no. 10, pp. 4525–4539, Oct. 2016.
- [20] J. Tye, P. Jales, M. Unwin, and C. Underwood, "The first application of stare processing to retrieve mean square slope using the SGR-ReSI GNSS-R experiment on TDS-1," *IEEE J. Sel. Topics Appl. Earth Observ. Remote Sens.*, vol. 9, no. 10, pp. 4669–4677, Oct. 2016.
- [21] C. Ruf et al., *CYGNSS Handbook Cyclone Global Navigation Satellite System: Deriving Surface Wind Speeds in Tropical Cyclones*. Ann Arbor, MI, USA: National Aeronautics and Space Administration, 2016, p. 154.
- [22] H. Carreno-Luengo et al., "3Cat-2—An experimental nanosatellite for GNSS-R earth observation: Mission concept and analysis," *IEEE J. Sel. Topics Appl. Earth Observ. Remote Sens.*, vol. 9, no. 10, pp. 4540–4551, Oct. 2016.
- [23] H. Carreno-Luengo, S. Lowe, C. Zuffada, S. Esterhuizen, and S. Oveisgharan, "Spaceborne GNSS-R from the SMAP mission: First assessment of polarimetric scatterometry over land and cryosphere," *Remote Sens.*, vol. 9, no. 4, 2017, Art. no. 362.
- [24] D. Masters, "Design and planning for the first spire GNSS-R missions of 2019," in *Proc. IEEE GRSS, Spec. Meeting Reflectometry Using GNSS Other Signals Opportunity*, 2019.
- [25] Y. Sun et al., "The status and progress of Fengyun-3E GNOS II mission for GNSS remote sensing," in *Proc. IEEE Int. Geosci. Remote Sens. Symp.*, 2019, pp. 5181–5184.
- [26] National Satellite Meteorological Center, 2023. [Online]. Available: <http://www.nsmc.org.cn/nsmc/cn/instrument/GNOS-2.html>
- [27] National Satellite Meteorological Center, 2023. [Online]. Available: <https://satellite.nsmc.org.cn/FY3G/html/IOTDATASET.html>
- [28] A. Camps et al., "FSSCAT, the 2017 Copernicus masters' 'ESA sentinel small satellite challenge' winner: A federated polar and soil moisture tandem mission based on 6U CubeSats," in *Proc. IEEE Int. Geosci. Remote Sens. Symp.*, 2018, pp. 8285–8287.
- [29] J. F. Munoz-Martin et al., "3Cat-4: Combined GNSS-R, L-Band radiometer with RFI mitigation, and AIS receiver for a I-Unit CubeSat based on software defined radio," in *Proc. IEEE Int. Geosci. Remote Sens. Symp.*, 2018, pp. 1063–1066.
- [30] NanoSat Lab, 2024. [Online]. Available: <https://nanosatlab.upc.edu/en-missions-and-projects/3cat-4>
- [31] A. Dielacher et al., "The ESA passive reflectometry and dosimetry (PRETTY) mission," in *Proc. IEEE Int. Geosci. Remote Sens. Symp.*, 2019, pp. 5173–5176.
- [32] J.-C. Juang, S.-H. Ma, and C.-T. Lin, "Study of GNSS-R techniques for FORMOSAT mission," *IEEE J. Sel. Topics Appl. Earth Observ. Remote Sens.*, vol. 9, no. 10, pp. 4582–4592, Oct. 2016.
- [33] M. J. Unwin et al., "An introduction to the HydroGNSS GNSS reflectometry remote sensing mission," *IEEE J. Sel. Topics Appl. Earth Observ. Remote Sens.*, vol. 14, pp. 6987–6999, 2021.
- [34] C. Ruf et al., "CYGNSS: Enabling the future of hurricane prediction [remote sensing satellites]," *IEEE Geosci. Remote Sens. Mag.*, vol. 1, no. 2, pp. 52–67, Jun. 2013.
- [35] M. P. Clarizia and C. S. Ruf, "Wind speed retrieval algorithm for the cyclone global navigation satellite system (CYGNSS) mission," *IEEE Trans. Geosci. Remote Sens.*, vol. 54, no. 8, pp. 4419–4432, Aug. 2016.

- [36] V. Freeman et al., "Earth surface monitoring with spire's new GNSS reflectometry (GNSS-R) CubeSats," in *Proc. EGU Gen. Assem. Conf. Abstr.*, 2020, Paper 13766.
- [37] D. Masters et al., "Status and plans for Spire's growing commercial constellation of GNSS science CubeSats," in *Proc. Joint 6th ROM SAF User Workshop 7th IROWG Workshop*, 2019, pp. 19–25.
- [38] P. Zhang et al., "FY-3E: The first operational meteorological satellite mission in an early morning orbit," *Adv. Atmospheric Sci.*, vol. 39, no. 1, pp. 1–8, 2022.
- [39] E. Cardellach et al., "First precise spaceborne sea surface altimetry with GNSS reflected signals," *IEEE J. Sel. Topics Appl. Earth Observ. Remote Sens.*, vol. 13, pp. 102–112, 2020.
- [40] A. M. Semmling et al., "Sea surface topography retrieved from GNSS reflectometry phase data of the GEOHALO flight mission," *Geophysical Res. Lett.*, vol. 41, no. 3, pp. 954–960, 2014.
- [41] H. Y. Wang and J. C. Juang, "Retrieval of ocean surface wind speed using reflected BPSK/BOC signals," *Remote Sens.*, vol. 12, no. 17, 2020, Art. no. 2698.
- [42] M. Unwin, J. Rawlinson, L. King, G. Foti, M. Hammond, and T. Burger, "GNSS-reflectometry activities on the DoT-1 microsatellite in preparation for the hydrognss mission," in *Proc. IEEE Int. Geosci. Remote Sens. Symp.*, 2021, pp. 1288–1290.
- [43] N. Fu and F. Li, "An introduction of GNSS reflectometer remote sensing mission from Yunyao Aerospace Technology Co., Ltd," in *Proc. IEEE Specialist Meeting Reflectometry using GNSS Other Signals Opportunity*, 2021, pp. 77–81.
- [44] C. Li and W. Huang, "An algorithm for sea-surface wind field retrieval from GNSS-R delay-Doppler map," *IEEE Geosci. Remote Sens. Lett.*, vol. 11, no. 12, pp. 2110–2114, Dec. 2014.
- [45] N. Rodriguez-Alvarez and J. L. Garrison, "Generalized linear observables for ocean wind retrieval from calibrated GNSS-R delay-Doppler maps," *IEEE Trans. Geosci. Remote Sens.*, vol. 54, no. 2, pp. 1142–1155, Feb. 2016.
- [46] J. Bu, K. Yu, Y. Zhu, N. Qian, and J. Chang, "Developing and testing models for sea surface wind speed estimation with GNSS-R delay Doppler maps and delay waveforms," *Remote Sens.*, vol. 12, no. 22, 2020, Art. no. 3760.
- [47] W. Guo, H. Du, J. W. Cheong, B. J. Southwell, and A. G. Dempster, "GNSS-R wind speed retrieval of sea surface based on particle swarm optimization algorithm," *IEEE Trans. Geosci. Remote Sens.*, vol. 60, 2022, Art. no. 4202414.
- [48] Y. Liu, I. Collett, and Y. J. Morton, "Application of neural network to GNSS-R wind speed retrieval," *IEEE Trans. Geosci. Remote Sens.*, vol. 57, no. 12, pp. 9756–9766, Dec. 2019.
- [49] J. Reynolds, M. P. Clarizia, and E. Santi, "Wind speed estimation from CYGNSS using artificial neural networks," *IEEE J. Sel. Topics Appl. Earth Observ. Remote Sens.*, vol. 13, pp. 708–716, 2020.
- [50] X. Li et al., "Analysis of coastal wind speed retrieval from CYGNSS mission using artificial neural network," *Remote Sens. Environ.*, vol. 260, 2021, Art. no. 112454.
- [51] X. Chu et al., "Multimodal deep learning for heterogeneous GNSS-R data fusion and ocean wind speed retrieval," *IEEE J. Sel. Topics Appl. Earth Observ. Remote Sens.*, vol. 13, pp. 5971–5981, 2020.
- [52] M. Asgarimehr, C. Arnold, T. Weigel, C. Ruf, and J. Wickert, "GNSS reflectometry global ocean wind speed using deep learning: Development and assessment of CyGNSSnet," *Remote Sens. Environ.*, vol. 269, 2022, Art. no. 112801.
- [53] W. Guo, H. Du, C. Guo, B. J. Southwell, J. W. Cheong, and A. G. Dempster, "Information fusion for GNSS-R wind speed retrieval using statistically modified convolutional neural network," *Remote Sens. Environ.*, vol. 272, 2022, Art. no. 112934.
- [54] J. Bu, K. Yu, X. Zuo, J. Ni, Y. Li, and W. Huang, "GloWS-Net: A deep learning framework for retrieving global sea surface wind speed using spaceborne GNSS-R data," *Remote Sens.*, vol. 15, no. 3, 2023, Art. no. 590.
- [55] X. X. Liu et al., "FA-RDN: A hybrid neural network on GNSS-R sea surface wind speed retrieval," *Remote Sens.*, vol. 13, no. 23, Dec. 2021, Art. no. 4820.
- [56] C. Lu, Z. Wang, Z. Wu, Y. Zheng, and Y. Liu, "Global ocean wind speed retrieval from GNSS reflectometry using CNN-LSTM network," *IEEE Trans. Geosci. Remote Sens.*, vol. 61, 2023, Art. no. 5801112.
- [57] C. S. Ruf and R. Balasubramanian, "Development of the CYGNSS geophysical model function for wind speed," *IEEE J. Sel. Topics Appl. Earth Observ. Remote Sens.*, vol. 12, no. 1, pp. 66–77, Jan. 2019.
- [58] D. Zhao et al., "DDM-former: Transformer networks for GNSS reflectometry global ocean wind speed estimation," *Remote Sens. Environ.*, vol. 294, 2023, Art. no. 113629.
- [59] J. Park and J. T. Johnson, "A study of wind direction effects on sea surface specular scattering for GNSS-R applications," *IEEE J. Sel. Topics Appl. Earth Observ. Remote Sens.*, vol. 10, no. 11, pp. 4677–4685, Nov. 2017.
- [60] J. Park and J. T. Johnson, "A study of wind direction effects on GNSS-R delay Doppler maps near the specular point," in *Proc. IEEE Int. Geosci. Remote Sens. Symp.*, 2017, pp. 1426–1429.
- [61] G. Zhang, D. Yang, Y. Yu, and F. Wang, "Wind direction retrieval using spaceborne GNSS-R in nonspherical geometry," *IEEE J. Sel. Topics Appl. Earth Observ. Remote Sens.*, vol. 13, pp. 649–658, 2020.
- [62] D. L. Guan et al., "Wind direction signatures in GNSS-R observables from space," *Remote Sens.*, vol. 10, no. 2, Feb. 2018, Art. no. 198.
- [63] F. Wang, D. Yang, and L. Yang, "Feasibility of wind direction observation using low-altitude global navigation satellite system-reflectometry," *IEEE J. Sel. Topics Appl. Earth Observ. Remote Sens.*, vol. 11, no. 12, pp. 5063–5075, Dec. 2018.
- [64] B. J. Southwell and N. Inst, "Investigating the sensitivity of delay Doppler maps to wind direction using ambiguous stare processing," in *Proc. 31st Int. Tech. Meeting Satell. Division Inst. Navigation*, 2018, pp. 2819–2833.
- [65] H. Gao, Z. Bai, and D. Fan, "A method of spaceborne GNSS-R sea surface wind direction inversion," *J. Astronaut.*, vol. 41, no. 11, pp. 1473–1480, 2020.
- [66] D. Pascual, M. P. Clarizia, and C. S. Ruf, "Spaceborne demonstration of GNSS-R scattering cross section sensitivity to wind direction," *IEEE Geosci. Remote Sens. Lett.*, vol. 19, 2022, Art. no. 8006005.
- [67] Y. Zhang et al., "Wind direction retrieval using support vector machine from CYGNSS sea surface data," *Remote Sens.*, vol. 13, no. 21, 2021, Art. no. 4451.
- [68] Y. Zhang et al., "Wind direction retrieval from CYGNSS L1 level sea surface data based on machine learning," *IEEE Trans. Geosci. Remote Sens.*, vol. 60, 2022, Art. no. 5804413.
- [69] F. Martín et al., "Typhoon observations using the interferometric GNSS-R technique," in *Proc. IEEE Geosci. Remote Sens. Symp.*, 2014, pp. 3790–3793.
- [70] W. Li, D. Yang, F. Fabra, Y. Cao, and W. Yang, *Typhoon Wind Speed Observation Utilizing Reflected Signals From Beidou GEO Satellites*. Berlin, Germany: Springer, 2014, pp. 191–200.
- [71] G. Foti, C. Gommenginger, and M. Srokosz, "First spaceborne GNSS-reflectometry observations of hurricanes from the U.K. TechDemoSat-1 mission," *Geophysical Res. Lett.*, vol. 44, no. 24, pp. 12358–12366, 2017.
- [72] M. Morris and C. S. Ruf, "Determining tropical cyclone surface wind speed structure and intensity with the CYGNSS satellite constellation," *J. Appl. Meteorol. Climatol.*, vol. 56, no. 7, pp. 1847–1865, 2017.
- [73] R. Balasubramanian and C. Ruf, "Azimuthal dependence of GNSS-R scattering cross-section in hurricanes," *J. Geophysical Res., Oceans*, vol. 125, no. 7, 2020, Art. no. e2020JC016167.
- [74] H. Shen, W. Perrie, and Y. He, "Evaluation of hurricane wind speed retrieval from cross-dual-pol SAR," *Int. J. Remote Sens.*, vol. 37, no. 3, pp. 599–614, 2016.
- [75] F. Said, S. J. Katzberg, and S. Soisuvarn, "Retrieving hurricane maximum winds using simulated CYGNSS power-versus-delay waveforms," *IEEE J. Sel. Topics Appl. Earth Observ. Remote Sens.*, vol. 10, no. 8, pp. 3799–3809, Aug. 2017.
- [76] S.-K. Kim and J. Park, "Monitoring a storm surge during Hurricane Harvey using multi-constellation GNSS-Reflectometry," *GPS Sol.*, vol. 25, no. 2, 2021, Art. no. 63.
- [77] S. Wang, S. Shi, and B. Ni, "Joint use of spaceborne microwave sensor data and CYGNSS data to observe tropical cyclones," *Remote Sens.*, vol. 12, no. 19, 2020, Art. no. 3124.
- [78] M. Morris and C. S. Ruf, "Estimating tropical cyclone integrated kinetic energy with the CYGNSS satellite constellation," *J. Appl. Meteorol. Climatol.*, vol. 56, no. 1, pp. 235–245, 2017.
- [79] D. Mayers and C. Ruf, "Tropical cyclone center fix using CYGNSS winds," *J. Appl. Meteorol. Climatol.*, vol. 58, no. 9, pp. 1993–2003, 2019.
- [80] C. Ruf et al., "In-orbit performance of the constellation of CYGNSS hurricane satellites," *Bull. Amer. Meteorological Soc.*, vol. 100, no. 10, pp. 2009–2023, 2019.
- [81] D. P. Chambers, J. C. Ries, C. K. Shum, and B. D. Tapley, "On the use of tide gauges to determine altimeter drift," *J. Geophysical Res., Oceans*, vol. 103, no. C6, pp. 12885–12890, 1998.

- [82] Y. Zhang et al., "Machine learning methods for spaceborne GNSS-R sea surface height measurement from TDS-1," *IEEE J. Sel. Topics Appl. Earth Observ. Remote Sens.*, vol. 15, pp. 1079–1088, 2022.
- [83] K. D. Anderson, "Determination of water level and tides using interferometric observations of GPS signals," *J. Atmospheric Ocean. Technol.*, vol. 17, no. 8, pp. 1118–1127, 2000.
- [84] D. Purnell, N. Gomez, N. H. Chan, J. Strandberg, D. M. Holland, and T. Hobiger, "Quantifying the uncertainty in ground-based GNSS-reflectometry sea level measurements," *IEEE J. Sel. Topics Appl. Earth Observ. Remote Sens.*, vol. 13, pp. 4419–4428, 2020.
- [85] J. S. Löfgren, R. Haas, and J. M. Johansson, "Monitoring coastal sea level using reflected GNSS signals," *Adv. Space Res.*, vol. 47, no. 2, pp. 213–220, 2011.
- [86] W. Li, E. Cardellach, F. Fabra, S. Ribó, and A. Rius, "Lake level and surface topography measured with spaceborne GNSS-reflectometry from CYGNSS mission: Example for the lake Qinghai," *Geophysical Res. Lett.*, vol. 45, no. 24, pp. 13332–13341, 2018.
- [87] W. Liu et al., "Coastal sea-level measurements based on GNSS-R phase altimetry: A case study at the Onsala Space Observatory, Sweden," *IEEE Trans. Geosci. Remote Sens.*, vol. 55, no. 10, pp. 5625–5636, Oct. 2017.
- [88] C. Hu, C. R. Benson, C. Rizos, and L. Qiao, "Impact of receiver dynamics on space-based GNSS-R altimetry," *IEEE J. Sel. Topics Appl. Earth Observ. Remote Sens.*, vol. 12, no. 6, pp. 1974–1980, Jun. 2019.
- [89] W. Li, A. Rius, F. Fabra, E. Cardellach, S. Ribo, and M. Martin-Neira, "Revisiting the GNSS-R waveform statistics and its impact on altimetric retrievals," *IEEE Trans. Geosci. Remote Sens.*, vol. 56, no. 5, pp. 2854–2871, May 2018.
- [90] M. Song et al., "Study on the exploration of spaceborne GNSS-R raw data focusing on altimetry," *IEEE J. Sel. Topics Appl. Earth Observ. Remote Sens.*, vol. 13, pp. 6142–6154, 2020.
- [91] J. Mashburn, P. Axelrad, S. T. Lowe, and K. M. Larson, "Global ocean altimetry with GNSS reflections from TechDemoSat-1," *IEEE Trans. Geosci. Remote Sens.*, vol. 56, no. 7, pp. 4088–4097, Jul. 2018.
- [92] J. Mashburn, P. Axelrad, C. Zuffada, E. Loria, A. O'Brien, and B. Haines, "Improved GNSS-R ocean surface altimetry with CYGNSS in the seas of Indonesia," *IEEE Trans. Geosci. Remote Sens.*, vol. 58, no. 9, pp. 6071–6087, Sep. 2020.
- [93] W. Li, E. Cardellach, F. Fabra, S. Ribo, and A. Rius, "Assessment of spaceborne GNSS-R ocean altimetry performance using CYGNSS mission raw data," *IEEE Trans. Geosci. Remote Sens.*, vol. 58, no. 1, pp. 238–250, Jan. 2020.
- [94] V. A. Nguyen, O. Nogués-Correig, T. Yuasa, D. Masters, and V. Irisov, "Initial GNSS phase altimetry measurements from the spire satellite constellation," *Geophysical Res. Lett.*, vol. 47, no. 15, 2020, Art. no. e2020GL088308.
- [95] Z. Cheng, T. Jin, X. Chang, Y. Li, and X. Wan, "Evaluation of spaceborne GNSS-R based sea surface altimetry using multiple constellation signals," *Front. Earth Sci.*, vol. 10, 2023, Art. no. 1079255.
- [96] Y. Zhang et al., "Global sea surface height measurement from CYGNSS based on machine learning," *IEEE J. Sel. Topics Appl. Earth Observ. Remote Sens.*, vol. 16, pp. 841–852, 2023.
- [97] Q. Wang, W. Zheng, F. Wu, A. Xu, H. Zhu, and Z. Liu, "A new GNSS-R altimetry algorithm based on machine learning fusion model and feature optimization to improve the precision of sea surface height retrieval," *Front. Earth Sci.*, vol. 9, 2021, Art. no. 730565.
- [98] Q. Wang et al., "Information fusion for spaceborne GNSS-R sea surface height retrieval using modified residual multimodal deep learning method," *Remote Sens.*, vol. 15, no. 6, 2023, Art. no. 1481.
- [99] Z. Liu, L. Du, P. Zhou, X. Wang, Z. Zhang, and Z. Liu, "Cloud-based near real-time sea level monitoring using GNSS reflectometry," *GPS Sol.*, vol. 27, no. 2, 2023, Art. no. 65.
- [100] E. Cardellach, C. O. Ao, M. de la Torre Juárez, and G. A. Hajj, "Carrier phase delay altimetry with GPS-reflection/occultation interferometry from low Earth orbiters," *Geophysical Res. Lett.*, vol. 31, no. 10, 2004, Art. no. L10402.
- [101] C. Jing et al., "A review of the BuFeng-1 GNSS-R mission: Calibration and validation results of sea surface and land surface," *Geo-Spatial Inf. Sci.*, pp. 1–15, 2024, doi: [10.1080/10095020.2024.2330547](https://doi.org/10.1080/10095020.2024.2330547).
- [102] S. Soisuvarn, Z. Jelenak, F. Said, P. S. Chang, and A. Egido, "The GNSS reflectometry response to the ocean surface winds and waves," *IEEE J. Sel. Topics Appl. Earth Observ. Remote Sens.*, vol. 9, no. 10, pp. 4678–4699, Oct. 2016.
- [103] J. C. Leader, "Incoherent backscatter from rough surfaces: The two-scale model reexamined," *Radio Sci.*, vol. 13, no. 3, pp. 441–457, 1978.
- [104] B. Li, L. Yang, B. Zhang, D. Yang, and D. Wu, "Modeling and simulation of GNSS-R observables with effects of swell," *IEEE J. Sel. Topics Appl. Earth Observ. Remote Sens.*, vol. 13, pp. 1833–1841, 2020.
- [105] J. Wang, L. Aouf, Y. Jia, and Y. Zhang, "Validation and calibration of significant wave height and wind speed retrievals from HY2B altimeter based on deep learning," *Remote Sens.*, vol. 12, no. 17, 2020, Art. no. 2858.
- [106] J. Yang, J. Zhang, Y. Jia, C. Fan, and W. Cui, "Validation of sentinel-3A/3B and Jason-3 altimeter wind speeds and significant wave heights using buoy and ASCAT data," *Remote Sens.*, vol. 12, no. 13, 2020, Art. no. 2079.
- [107] F. Soulard, M. Caparrini, O. Germain, P. Lopez-Dekker, M. Taani, and G. Ruffini, "Sea state monitoring using coastal GNSS-R," *Geophysical Res. Lett.*, vol. 31, no. 21, 2004, Art. no. L21303.
- [108] A. Alonso-Arroyo, A. Camps, H. Park, D. Pascual, R. Onrubia, and F. Martín, "Retrieval of significant wave height and mean sea surface level using the GNSS-R interference pattern technique: Results from a three-month field campaign," *IEEE Trans. Geosci. Remote Sens.*, vol. 53, no. 6, pp. 3198–3209, Jun. 2015.
- [109] Q. Peng and S. G. Jin, "Significant wave height estimation from spaceborne cyclone-GNSS reflectometry," *Remote Sens.*, vol. 11, no. 5, 2019, Art. no. 584.
- [110] L. Qin and Y. Li, "Significant wave height estimation using multi-satellite observations from GNSS-R," *Remote Sens.*, vol. 13, 2021, Art. no. 4806.
- [111] S. Yang, S. Jin, Y. Jia, and M. Ye, "Significant wave height estimation from joint CYGNSS DDMA and LES observations," *Sensors*, vol. 21, no. 18, 2021, Art. no. 6123.
- [112] J. Bu and K. Yu, "Significant wave height retrieval method based on spaceborne GNSS reflectometry," *IEEE Geosci. Remote Sens. Lett.*, vol. 19, 2022, Art. no. 1503705.
- [113] C. Wang, K. Yu, K. Zhang, J. Bu, and F. Qu, "Significant wave height retrieval based on multivariable regression models developed with CYGNSS data," *IEEE Trans. Geosci. Remote Sens.*, vol. 61, 2023, Art. no. 4200415.
- [114] F. Wang, D. Yang, J. Wang, J. Xing, and Y. Yu, "Shipborne GNSS reflectometry for monitoring along-track significant wave height and wind speed," *Ocean Eng.*, vol. 281, 2023, Art. no. 114935.
- [115] J. Bu, K. Yu, F. Zhu, X. Zuo, and W. Huang, "Joint retrieval of sea surface rainfall intensity, wind speed, and wave height based on spaceborne GNSS-R: A case study of the oceans near China," *Remote Sens.*, vol. 15, no. 11, 2023, Art. no. 2757.
- [116] X. Wang, X. He, J. Shi, S. Chen, and Z. Niu, "Estimating sea level, wind direction, significant wave height, and wave peak period using a geodetic GNSS receiver," *Remote Sens. Environ.*, vol. 279, 2022, Art. no. 113135.
- [117] L. Qin and Y. Li, "Significant wave height estimation using multi-satellite observations from GNSS-R," *Remote Sens.*, vol. 13, no. 23, 2021, Art. no. 4806.
- [118] W. Shibo, Y. Li, M. Xie, and M. Hou, "Inversion method of significant wave height based on time delay window using the ship-borne Beidou reflected signal," *Ocean Eng.*, vol. 272, 2023, Art. no. 113815.
- [119] J. Bu, H. Park, K. Yu, and A. Camps, "Estimation of significant wave height using the features of CYGNSS delay Doppler map," in *Proc. IEEE Int. Geosci. Remote Sens. Symp.*, 2022, pp. 7639–7642.
- [120] J. Bu and K. Yu, "A new integrated method of CYGNSS DDMA and LES measurements for significant wave height estimation," *IEEE Geosci. Remote Sens. Lett.*, vol. 19, 2022, Art. no. 1505605.
- [121] S. Durden and J. Vesely, "A physical radar cross-section model for a wind-driven sea with swell," *IEEE J. Ocean. Eng.*, vol. 10, no. 4, pp. 445–451, Oct. 1985.
- [122] A. Ghavidel and A. Camps, "Impact of rain, swell, and surface currents on the electromagnetic bias in GNSS-reflectometry," *IEEE J. Sel. Topics Appl. Earth Observ. Remote Sens.*, vol. 9, no. 10, pp. 4643–4649, Oct. 2016.
- [123] J. Albuquerque, J. A. A. Antolínez, A. Rueda, F. J. Méndez, and G. Coco, "Directional correction of modeled sea and swell wave heights using satellite altimeter data," *Ocean Model.*, vol. 131, pp. 103–114, 2018.
- [124] X. M. Li, "A new insight from space into swell propagation and crossing in the global oceans," *Geophysical Res. Lett.*, vol. 43, no. 10, pp. 5202–5209, May 2016.
- [125] O. Altiparmaki, M. Kleinenhenbrink, M. Naeije, C. Slobbe, and P. Visser, "SAR Altimetry data as a new source for swell monitoring," *Geophysical Res. Lett.*, vol. 49, no. 7, 2022, Art. no. e2021GL096224.

- [126] C. Shen, E. Gill, and W. Huang, "Extraction of swell parameters from simulated noisy HF radar signals," in *Proc. IEEE Radar Conf.*, 2013, pp. 1–6.
- [127] W. Wang, P. Forget, and C. Guan, "Inversion and assessment of swell waveheights from HF radar spectra in the Iroise Sea," *Ocean Dyn.*, vol. 66, no. 4, pp. 527–538, 2016.
- [128] K. W. Gurgel, H. H. Essen, and S. P. Kingsley, "High-frequency radars: Physical limitations and recent developments," *Coastal Eng.*, vol. 37, no. 3, pp. 201–218, 1999.
- [129] J. Bu et al., "Estimation of swell height using spaceborne GNSS-R data from eight CYGNSS satellites," *Remote Sens.*, vol. 14, no. 18, 2022, Art. no. 4634.
- [130] J. Bu, K. Yu, J. Ni, and W. Huang, "Combining ERA5 data and CYGNSS observations for the joint retrieval of global significant wave height of ocean swell and wind wave: A deep convolutional neural network approach," *J. Geodesy*, vol. 97, no. 8, 2023, Art. no. 81.
- [131] Z. R. Alattabi, D. Cahill, and G. Voulgaris, "Swell and wind wave inversion using a single very high frequency (VHF) radar," *J. Atmospheric Ocean. Technol.*, vol. 36, no. 6, pp. 987–1013, 2019.
- [132] X. Liu, W. Huang, and E. W. Gill, "Estimation of significant wave height from X-band marine radar images based on ensemble empirical mode decomposition," *IEEE Geosci. Remote Sens. Lett.*, vol. 14, no. 10, pp. 1740–1744, Oct. 2017.
- [133] Y. Zhu, C. Shen, G. Zhang, Y. Zhao, F. Liu, and Y. Xu, "Rethinking the development of earthquake monitoring and prediction in mobile gravity," *J. Geodesy Geodyn.*, vol. 38, no. 5, pp. 441–446, 2018.
- [134] S. C. Zhang, X. R. Chen, Y. Nan, and Q. Liu, "Monitoring the study of offshore sea level changes with GPS-MR technology," in *Proc. China Satell. Navigation Conf.*, 2019, pp. 31–39.
- [135] C. Rong, H. Jian, W. A. N. Qilin, Y. I. Yanming, and L. V. Weihua, "An overview on the construction and observation progress of marine meteorological science experiment base at Bohe, Maoming," *J. Trop. Meteorol.*, vol. 27, no. 3, pp. 417–426, 2011.
- [136] R. Stosius, G. Beyerle, A. Helm, A. Hoechner, and J. Wickert, "Simulation of space-borne tsunami detection using GNSS-Reflectometry applied to tsunamis in the Indian Ocean," *Natural Hazards Earth Syst. Sci.*, vol. 10, no. 6, pp. 1359–1372, 2010.
- [137] R. Stosius, G. Beyerle, A. Hoechner, J. Wickert, and J. Lauterjung, "The impact on tsunami detection from space using GNSS-reflectometry when combining GPS with GLONASS and Galileo," *Adv. Space Res.*, vol. 47, no. 5, pp. 843–853, 2011.
- [138] Q. Yan and W. Huang, "GNSS-R delay-Doppler map simulation based on the 2004 Sumatra-Andaman tsunami event," *J. Sensors*, vol. 2016, no. 1, 2016, Art. no. 2750862.
- [139] Q. Yan and W. Huang, "Tsunami detection and parameter estimation from GNSS-R delay-Doppler map," *IEEE J. Sel. Topics Appl. Earth Observ. Remote Sens.*, vol. 9, no. 10, pp. 4650–4659, Oct. 2016.
- [140] K. Yu, "Weak tsunami detection using GNSS-R-based sea surface height measurement," *IEEE Trans. Geosci. Remote Sens.*, vol. 54, no. 3, pp. 1363–1375, Mar. 2016.
- [141] K. Yu, "Simplified tsunami modeling and waveform reconstruction with GNSS-R observations," *IEEE Trans. Aerosp. Electron. Syst.*, vol. 54, no. 3, pp. 1470–1484, Jun. 2018.
- [142] S.-K. Kim, E. Lee, J. Park, and S. Shin, "Feasibility analysis of GNSS-reflectometry for monitoring coastal hazards," *Remote Sens.*, vol. 13, no. 5, Mar. 2021, Art. no. 976.
- [143] J. S. Löfgren and R. Haas, "Sea level measurements using multi-frequency GPS and GLONASS observations," *EURASIP J. Adv. Signal Process.*, vol. 2014, no. 1, 2014, Art. no. 50.
- [144] P. L. Vu et al., "Identifying 2010 xynthia storm signature in GNSS-R-based tide records," *Remote Sens.*, vol. 11, no. 7, 2019, Art. no. 782.
- [145] D. Peng, E. M. Hill, L. Li, A. D. Switzer, and K. M. Larson, "Application of GNSS interferometric reflectometry for detecting storm surges," *GPS Sol.*, vol. 23, no. 2, 2019, Art. no. 47.
- [146] X. Li et al., "Exploiting the potential of coastal GNSS-R for improving storm surge modeling," *IEEE Geosci. Remote Sens. Lett.*, vol. 18, no. 7, pp. 1134–1138, Jul. 2021.
- [147] A. Komjathy, J. Maslanik, V. U. Zavorotny, P. Axelrad, and S. J. Katzberg, "Sea ice remote sensing using surface reflected GPS signals," in *Proc. IEEE Int. Geosci. Remote Sens. Symp. Taking Pulse Planet: Role Remote Sens. Manag. Environ.*, 2000, vol. 7, pp. 2855–2857.
- [148] M. Wiehl, B. Legresy, and R. Dietrich, "Potential of reflected GNSS signals for ice sheet remote sensing - Abstract," *J. Electromagn. Waves Appl.*, vol. 17, no. 7, pp. 1045–1047, 2003.
- [149] M. B. Rivas, J. A. Maslanik, and P. Axelrad, "Bistatic scattering of GPS signals off arctic sea ice," *IEEE Trans. Geosci. Remote Sens.*, vol. 48, no. 3, pp. 1548–1553, Mar. 2010.
- [150] J. F. Marchan-Hernandez, N. Rodriguez-Alvarez, A. Camps, X. Bosch-Lluis, I. Ramos-Perez, and E. Valencia, "Correction of the sea state impact in the L-band brightness temperature by means of delay-Doppler maps of global navigation satellite signals reflected over the sea surface," *IEEE Trans. Geosci. Remote Sens.*, vol. 46, no. 10, pp. 2914–2923, Oct. 2008.
- [151] N. Rodriguez-Alvarez, D. M. Akos, V. U. Zavorotny, J. A. Smith, A. Camps, and C. W. Fairall, "Airborne GNSS-R wind retrievals using delay-Doppler maps," *IEEE Trans. Geosci. Remote Sens.*, vol. 51, no. 1, pp. 626–641, Jan. 2013.
- [152] A. Alonso-Arroyo, V. U. Zavorotny, and A. Camps, "Sea ice detection using U.K. TD_S-1 GNSS-R data," *IEEE Trans. Geosci. Remote Sens.*, vol. 55, no. 9, pp. 4989–5001, Sep. 2017.
- [153] Y. Zhu, K. Yu, J. Zou, and J. Wickert, "Sea ice detection based on differential delay-Doppler maps from U.K. TechDemoSat-1," *Sensors*, vol. 17, no. 7, Jul. 2017, Art. no. 1614.
- [154] Y. Zhu et al., "Sensing sea ice based on Doppler spread analysis of spaceborne GNSS-R data," *IEEE J. Sel. Topics Appl. Earth Observ. Remote Sens.*, vol. 13, pp. 217–226, 2020.
- [155] Q. Yan and W. Huang, "Spaceborne GNSS-R sea ice detection using delay-Doppler maps: First results from the U.K. TechDemoSat-1 mission," *IEEE J. Sel. Topics Appl. Earth Observ. Remote Sens.*, vol. 9, no. 10, pp. 4795–4801, Oct. 2016.
- [156] Y. Zhu et al., "Machine learning-aided sea ice monitoring using feature sequences extracted from spaceborne GNSS-reflectometry data," *Remote Sens.*, vol. 12, no. 22, 2020, Art. no. 3751.
- [157] Q. Yan and W. Huang, "Sea ice sensing from GNSS-R data using convolutional neural networks," *IEEE Geosci. Remote Sens. Lett.*, vol. 15, no. 10, pp. 1510–1514, Oct. 2018.
- [158] Q. Yan, W. Huang, and C. Moloney, "Neural networks based sea ice detection and concentration retrieval from GNSS-R delay-Doppler maps," *IEEE J. Sel. Topics Appl. Earth Observ. Remote Sens.*, vol. 10, no. 8, pp. 3789–3798, Aug. 2017.
- [159] D. Llaveria, J. F. Munoz-Martin, C. Herbert, M. Pablos, H. Park, and A. Camps, "Sea ice concentration and sea ice extent mapping with L-band microwave radiometry and GNSS-R data from the FFSCat mission using neural networks," *Remote Sens.*, vol. 13, no. 6, 2021, Art. no. 1139.
- [160] Q. Yan and W. Huang, "Detecting sea ice from TechDemoSat-1 data using support vector machines with feature selection," *IEEE J. Sel. Topics Appl. Earth Observ. Remote Sens.*, vol. 12, no. 5, pp. 1409–1416, May 2019.
- [161] Y. Hu, Z. Jiang, W. Liu, X. Yuan, Q. Hu, and J. Wickert, "GNSS-R sea ice detection based on linear discriminant analysis," *IEEE Trans. Geosci. Remote Sens.*, vol. 61, 2023, Art. no. 5800812.
- [162] C. Yin et al., "Sea ice detection with FY3E GNOS II GNSS reflectometry," in *Proc. IEEE Spec. Meeting Reflectometry Using GNSS Other Signals Opportunity*, 2021, pp. 36–38.
- [163] S. Gleason, "Towards sea ice remote sensing with space detected GPS signals: Demonstration of technical feasibility and initial consistency check using low resolution sea ice information," *Remote Sens.*, vol. 2, no. 8, pp. 2017–2039, 2010.
- [164] A. M. Semmling et al., "Sea-ice concentration derived from GNSS reflection measurements in Fram strait," *IEEE Trans. Geosci. Remote Sens.*, vol. 57, no. 12, pp. 10350–10361, Dec. 2019.
- [165] A. M. Semmling et al., "Sea-ice permittivity derived from GNSS reflection profiles: Results of the MOSAiC expedition," *IEEE Trans. Geosci. Remote Sens.*, vol. 60, 2022, Art. no. 4302416.
- [166] J. F. Munoz-Martin et al., "Snow and ice thickness retrievals using GNSS-R: Preliminary results of the MOSAiC experiment," *Remote Sens.*, vol. 12, no. 24, 2020, Art. no. 4038.
- [167] Y. Zhu, T. Tao, J. Zou, K. Yu, J. Wickert, and M. Semmling, "Spaceborne GNSS reflectometry for retrieving sea ice concentration using TDS-1 data," *IEEE Geosci. Remote Sens. Lett.*, vol. 18, no. 4, pp. 612–616, Apr. 2021.
- [168] L. Yang, B. Guo, Z. Zhang, and X. Zhang, "DNN-based retrieval of arctic sea ice concentration from GNSS-R and its effects on the synoptic-scale forecasting as supplementary observation source," *Geophysical Res. Lett.*, vol. 50, no. 14, 2023, Art. no. e2023GL104219.
- [169] S. Laxon, N. Peacock, and D. Smith, "High interannual variability of sea ice thickness in the Arctic region," *Nature*, vol. 425, no. 6961, pp. 947–950, 2003.

- [170] K. A. Giles, S. W. Laxon, and A. L. Ridout, "Circumpolar thinning of Arctic sea ice following the 2007 record ice extent minimum," *Geophysical Res. Lett.*, vol. 35, no. 22, 2008, Art. no. L22502.
- [171] X. Tian-Kunze et al., "SMOS-derived thin sea ice thickness: Algorithm baseline, product specifications and initial verification," *Cryosphere*, vol. 8, no. 3, pp. 997–1018, 2014.
- [172] M. Huntemann, G. Heygster, L. Kaleschke, T. Krumpen, M. Mäkynen, and M. Drusch, "Empirical sea ice thickness retrieval during the freeze-up period from SMOS high incident angle observations," *Cryosphere*, vol. 8, no. 2, pp. 439–451, 2014.
- [173] Q. Yan and W. Huang, "Sea ice thickness estimation from TechDemoSat-1 and soil moisture ocean salinity data using machine learning methods," in *Proc. Glob. Oceans, Singap. – U.S. Gulf Coast*, 2020, pp. 1–5.
- [174] Q. Yan and W. Huang, "Sea ice thickness measurement using spaceborne GNSS-R: First results with TechDemoSat-1 data," *IEEE J. Sel. Topics Appl. Earth Observ. Remote Sens.*, vol. 13, pp. 577–587, 2020.
- [175] C. Herbert, J. F. Munoz-Martin, D. Llaveria, M. Pablos, and A. Camps, "Sea ice thickness estimation based on regression neural networks using L-band microwave radiometry data from the FSSCat mission," *Remote Sens.*, vol. 13, no. 7, 2021, Art. no. 1366.
- [176] Y. Xie and Q. Yan, "Stand-alone retrieval of sea ice thickness from FY-3E GNOS-R data," *IEEE Geosci. Remote Sens. Lett.*, vol. 21, 2024, Art. no. 2000305.
- [177] H. Li, Q. Yan, and W. Huang, "Retrieval of sea ice thickness from FY-3E data using random forest method," *Adv. Space Res.*, vol. 74, no. 1, pp. 130–144, 2024.
- [178] L. F. Bliven, P. W. Sobieski, and C. Craeye, "Rain generated ring-waves: Measurements and modelling for remote sensing," *Int. J. Remote Sens.*, vol. 18, no. 1, pp. 221–228, 1997.
- [179] B. Lund, H. C. Graber, and R. Romeiser, "Wind retrieval from shipborne nautical X-band radar data," *IEEE Trans. Geosci. Remote Sens.*, vol. 50, no. 10, pp. 3800–3811, Oct. 2012.
- [180] X. Chen, W. Huang, C. Zhao, and Y. Tian, "Rain detection from X-band marine radar images: A support vector machine-based approach," *IEEE Trans. Geosci. Remote Sens.*, vol. 58, no. 3, pp. 2115–2123, Mar. 2020.
- [181] Y. Zheng, Z. Shi, Z. Lu, and W. Ma, "A method for detecting rainfall from X-band marine radar images," *IEEE Access*, vol. 8, pp. 19046–19057, 2020.
- [182] Z. Lu, L. Sun, and Y. Zhou, "A method for rainfall detection and rainfall intensity level retrieval from X-band marine radar images," *Appl. Sci.*, vol. 11, no. 4, 2021, Art. no. 1565.
- [183] Z. Duan, J. Liu, Y. Tuo, G. Chiogna, and M. Disse, "Evaluation of eight high spatial resolution gridded precipitation products in Adige Basin (Italy) at multiple temporal and spatial scales," *Sci. Total Environ.*, vol. 573, pp. 1536–1553, 2016.
- [184] S. Rana, J. McGregor, and J. Renwick, "Precipitation seasonality over the Indian subcontinent: An evaluation of gauge, reanalyses, and satellite retrievals," *J. Hydrometeorol.*, vol. 16, no. 2, pp. 631–651, 2015.
- [185] C. Yu, D. Hu, M. Liu, S. Wang, and Y. Di, "Spatio-temporal accuracy evaluation of three high-resolution satellite precipitation products in China area," *Atmospheric Res.*, vol. 241, 2020, Art. no. 104952.
- [186] M. Yang, G. Liu, T. Chen, Y. Chen, and C. Xia, "Evaluation of GPM IMERG precipitation products with the point rain gauge records over Sichuan, China," *Atmospheric Res.*, vol. 246, 2020, Art. no. 105101.
- [187] M. S. Keikhosravi Kiany, S. A. Masoodian, R. C. Balling Jr, and M. Montazeri, "Evaluation of the TRMM 3B42 product for extreme precipitation analysis over southwestern Iran," *Adv. Space Res.*, vol. 66, no. 9, pp. 2094–2112, 2020.
- [188] H. Chen, B. Yong, Y. Shen, J. Liu, Y. Hong, and J. Zhang, "Comparison analysis of six purely satellite-derived global precipitation estimates," *J. Hydrol.*, vol. 581, 2020, Art. no. 124376.
- [189] W. Tian, L. Yi, W. Liu, W. Huang, G. Ma, and Y. Zhang, "Ground radar precipitation estimation with deep learning approaches in meteorological private cloud," *J. Cloud Comput.*, vol. 9, no. 1, 2020, Art. no. 22.
- [190] G. Tang, M. P. Clark, S. M. Papalexiou, Z. Ma, and Y. Hong, "Have satellite precipitation products improved over last two decades? A comprehensive comparison of GPM IMERG with nine satellite and reanalysis datasets," *Remote Sens. Environ.*, vol. 240, 2020, Art. no. 111697.
- [191] A. Hamza et al., "Assessment of IMERG-V06, TRMM-3B42V7, SM2RAIN-ASCAT, and PERSIANN-CDR precipitation products over the Hindu Kush Mountains of Pakistan, South Asia," *Remote Sens.*, vol. 12, no. 23, 2020, Art. no. 3871.
- [192] Y. Zhang, G. Hanati, S. Danierhan, Q. Liu, and Z. Xu, "Evaluation and comparison of daily GPM/TRMM precipitation products over the Tianshan Mountains in China," *Water*, vol. 12, no. 11, 2020, Art. no. 3088.
- [193] M. Asgarimehr, V. Zavorotny, J. Wickert, and S. Reich, "Can GNSS reflectometry detect precipitation over oceans?," *Geophysical Res. Lett.*, vol. 45, no. 22, pp. 12585–12592, 2018.
- [194] R. Balasubramaniam and C. Ruf, "Characterization of rain impact on L-Band GNSS-R ocean surface measurements," *Remote Sens. Environ.*, vol. 239, 2020, Art. no. 111607.
- [195] J. Bu and K. Yu, "Sea surface rainfall detection and intensity retrieval based on GNSS-reflectometry data from the CYGNSS mission," *IEEE Trans. Geosci. Remote Sens.*, vol. 60, 2022, Art. no. 5802015.
- [196] J. Bu, K. Yu, S. Han, N. Qian, Y. Lin, and J. Wang, "Retrieval of sea surface rainfall intensity using spaceborne GNSS-R data," *IEEE Trans. Geosci. Remote Sens.*, vol. 60, 2022, Art. no. 5803116.
- [197] J. Bu et al., "Machine learning-based methods for sea surface rainfall detection from CYGNSS delay-Doppler maps," *GPS Sol.*, vol. 26, no. 4, 2022, Art. no. 132.
- [198] Q. Zhang, Y. Liu, and J. Xia, "Space-borne GNSS-R ionospheric delay error elimination by optimal spatial filtering," *Sensors*, vol. 20, no. 19, 2020, Art. no. 5535.
- [199] J. M. Pallares, G. Ruffini, and L. Ruffini, "Ionospheric tomography using GNSS reflections," *IEEE Trans. Geosci. Remote Sens.*, vol. 43, no. 2, pp. 321–326, Feb. 2005.
- [200] Y. Wang and Y. J. Morton, "Ionospheric total electron content and disturbance observations from space-borne coherent GNSS-R measurements," *IEEE Trans. Geosci. Remote Sens.*, vol. 60, 2022, Art. no. 5801013.
- [201] X. Ren, H. Liu, J. Zhang, D. Mei, and X. Zhang, "An improved method for ionospheric TEC estimation using the spaceborne GNSS-R observations," *IEEE Trans. Geosci. Remote Sens.*, vol. 60, 2022, Art. no. 5803812.
- [202] X. Ren et al., "Leveraging the CYGNSS spaceborne GNSS-R observations to detect ionospheric irregularities over the oceans: Method and verification," *Space Weather-Int. J. Res. Appl.*, vol. 20, no. 11, 2022, Art. no. e2022SW003141.
- [203] C. Molina and A. Camps, "First evidences of ionospheric plasma depletions observations using GNSS-R data from CYGNSS," *Remote Sens.*, vol. 12, no. 22, 2020, Art. no. 3782.
- [204] L. Liu, Y. J. Morton, Y. Wang, and K.-B. Wu, "Arctic TEC mapping using integrated LEO-based GNSS-R and ground-based GNSS observations: A simulation study," *IEEE Trans. Geosci. Remote Sens.*, vol. 60, 2022, Art. no. 5802410.
- [205] Y. Wang and Y. J. Morton, "River slope observation from spaceborne GNSS-R carrier phase measurements: A case study," *IEEE Geosci. Remote Sens. Lett.*, vol. 19, 2022, Art. no. 1503105.
- [206] J. Font, G. S. E. Lagerloef, D. M. Le Vine, A. Camps, and O.-Z. Zanife, "The determination of surface salinity with the European SMOS space mission," *IEEE Trans. Geosci. Remote Sens.*, vol. 42, no. 10, pp. 2196–2205, Oct. 2004.
- [207] Y. H. Kerr, P. Waldteufel, J.-P. Wigneron, J. Martinuzzi, J. Font, and M. Berger, "Soil moisture retrieval from space: The soil moisture and ocean salinity (SMOS) mission," *IEEE Trans. Geosci. Remote Sens.*, vol. 39, no. 8, pp. 1729–1735, Aug. 2001.
- [208] A. Camps et al., "The WISE 2000 and 2001 field experiments in support of the SMOS mission: Sea surface L-band brightness temperature observations and their application to sea surface salinity retrieval," *IEEE Trans. Geosci. Remote Sens.*, vol. 42, no. 4, pp. 804–823, Apr. 2004.
- [209] R. Sabia, A. Camps, M. Vall-Llossera, and N. Reul, "Impact on sea surface salinity retrieval of different auxiliary data within the SMOS mission," *IEEE Trans. Geosci. Remote Sens.*, vol. 44, no. 10, pp. 2769–2778, Oct. 2006.
- [210] R. Sabia, A. Camps, M. Vall-llossera, M. Talone, and J. Font, "Towards an ocean salinity error budget estimation within the SMOS mission," in *Proc. IEEE Int. Geosci. Remote Sens. Symp.*, 2007, pp. 38–41.
- [211] A. Camps, M. Caparrini, R. Sabia, and G. Ruffini, "Sea surface salinity retrieval from space: Potential synergistic use of GNSS-R signals to improve the sea state correction and application to the SMOS mission," in *Proc. IEEE MicroRad*, 2006, pp. 91–96.
- [212] R. Sabia, M. Caparrini, and G. Ruffini, "Potential synergistic use of GNSS-R signals to improve the sea-state correction in the sea surface salinity estimation: Application to the SMOS mission," *IEEE Trans. Geosci. Remote Sens.*, vol. 45, no. 7, pp. 2088–2097, Jul. 2007.

- [213] J. F. Marchan-Hernandez et al., "Ground-based GNSS-R measurements with the PAU instrument and their application to the sea surface salinity retrieval: First results," in *Proc. IEEE Int. Geosci. Remote Sens. Symp.*, 2008, pp. 530–533.
- [214] E. Valencia, A. Camps, N. Rodriguez-Alvarez, I. Ramos-Perez, X. Bosch-Lluis, and H. Park, "Improving the accuracy of sea surface salinity retrieval using GNSS-R data to correct the sea state effect," *Radio Sci.*, vol. 46, no. 6, pp. 1–11, Dec. 2011.
- [215] J. Kainulainen, K. Rautiainen, J. Lemmettyinen, M. T. Hallikainen, F. Martin-Porqueras, and M. Martin-Neira, "Detection of a sea surface salinity gradient using data sets of airborne synthetic aperture radiometer HUT-2-D and a GNSS-R instrument," *IEEE Trans. Geosci. Remote Sens.*, vol. 49, no. 11, pp. 4561–4571, Nov. 2011.
- [216] D. M. Le Vine, G. S. E. Lagerloef, and S. E. Torrusio, "Aquarius and remote sensing of sea surface salinity from space," *Proc. IEEE*, vol. 98, no. 5, pp. 688–703, May 2010.
- [217] E. Valencia et al., "On the use of GNSS-R data to correct L-band brightness temperatures for sea-state effects: Results of the ALBATROSS field experiments," *IEEE Trans. Geosci. Remote Sens.*, vol. 49, no. 9, pp. 3225–3235, Sep. 2011.
- [218] E. Dinmat, D. Le Vine, J. Boutin, T. Meissner, and G. Lagerloef, "Remote sensing of sea surface salinity: Comparison of satellite and in situ observations and impact of retrieval parameters," *Remote Sens.*, vol. 11, no. 7, 2019, Art. no. 750.
- [219] A. G. Fore, S. H. Yueh, W. Tang, B. W. Stiles, and A. K. Hayashi, "Combined active/passive retrievals of ocean vector wind and sea surface salinity with SMAP," *IEEE Trans. Geosci. Remote Sens.*, vol. 54, no. 12, pp. 7396–7404, Dec. 2016.
- [220] N. Sharma, "Retrieval of sea surface salinity from SMAP L-band radiometer: A novel approach for wind speed correction," *Quart. J. Roy. Meteorological Soc.*, vol. 145, no. 725, pp. 3455–3465, 2019.
- [221] J. F. Munoz-Martin and A. Camps, "Sea surface salinity and wind speed retrievals using GNSS-R and L-band microwave radiometry data from FMPL-2 onboard the FSSCat mission," *Remote Sens.*, vol. 13, no. 16, 2021, Art. no. 3224.
- [222] B. Liu et al., "First assessment of CyGNSS-incorporated SMAP sea surface salinity retrieval over pan-tropical ocean," *IEEE J. Sel. Topics Appl. Earth Observ. Remote Sens.*, vol. 14, pp. 12163–12173, 2021.
- [223] B. Liu, W. Wan, and Y. Hong, "Can the accuracy of sea surface salinity measurement be improved by incorporating spaceborne GNSS-reflectometry?," *IEEE Geosci. Remote Sens. Lett.*, vol. 18, no. 1, pp. 3–7, Jan. 2021.
- [224] E. Olmedo et al., "Empirical characterization of the SMOS brightness temperature bias and uncertainty for improving sea surface salinity retrieval," *IEEE J. Sel. Topics Appl. Earth Observ. Remote Sens.*, vol. 12, no. 7, pp. 2486–2503, Jul. 2019.
- [225] S. Rajabi-Kiasari and M. Hasanolou, "An efficient model for the prediction of SMAP sea surface salinity using machine learning approaches in the Persian Gulf," *Int. J. Remote Sens.*, vol. 41, no. 8, pp. 3221–3242, 2020.
- [226] E. Jang, Y. J. Kim, J. Im, and Y.-G. Park, "Improvement of SMAP sea surface salinity in river-dominated oceans using machine learning approaches," *GIScience Remote Sens.*, vol. 58, no. 1, pp. 138–160, 2021.
- [227] E. Jang, Y. J. Kim, J. Im, Y.-G. Park, and T. Sung, "Global sea surface salinity via the synergistic use of SMAP satellite and HYCOM data based on machine learning," *Remote Sens. Environ.*, vol. 273, 2022, Art. no. 112980.
- [228] Z. Li, F. Guo, Z. Zhang, and X. Zhang, "Correction of the SMAP sea surface brightness temperature and retrieval of sea surface salinity incorporating CYGNSS observables," *IEEE J. Sel. Topics Appl. Earth Observ. Remote Sens.*, vol. 17, pp. 3226–3235, 2024.
- [229] Z. Qiu, H. Xi, and Y. He, "Red tide detection in the east China seas based on AVHRR and MODIS data," in *Proc. IEEE Int. Symp. Geosci. Remote Sens.*, 2006, pp. 3390–3393.
- [230] M. Kahru, B. G. Michell, A. Diaz, and M. Miura, "MODIS detects a devastating algal bloom in Paracas Bay, Peru," *Eos, Trans. Amer. Geophysical Union*, vol. 85, no. 45, pp. 465–472, 2004.
- [231] Y. Kim, S. Kim, H. Park, J. Choi, and H. Lee, "In-situ test of red tide monitoring using microwave and millimeter-wave radiometer," in *Proc. IEEE Int. Geosci. Remote Sens. Symp.*, 2004, vol. 3, pp. 1911–1913.
- [232] N. Rodriguez-Alvarez and K. Oudrhiri, "The bistatic radar as an effective tool for detecting and monitoring the presence of phytoplankton on the ocean surface," *Remote Sens.*, vol. 13, no. 12, 2021, Art. no. 2248.
- [233] W. Ban, K. Zhang, K. Yu, N. Zheng, and S. Chen, "Detection of red tide over sea surface using GNSS-R spaceborne observations," *IEEE Trans. Geosci. Remote Sens.*, vol. 60, 2022, Art. no. 5802911.
- [234] W. Ban, N. Zheng, K. Yu, K. Zhang, and J. Liu, "Sea surface green algae density estimation using ship-borne GEO-satellite reflection observations," *IEEE Geosci. Remote Sens. Lett.*, vol. 19, 2022, Art. no. 5003205.
- [235] W. Ban, N. Zheng, K. Zhang, K. Yu, S. Chen, and Q. Lu, "Green algae monitoring via ground-based GNSS-R observations," *GPS Sol.*, vol. 27, no. 1, 2022, Art. no. 36.
- [236] Y. Zhen and Q. Yan, "Improving spaceborne GNSS-R algal bloom detection with meteorological data," *Remote Sens.*, vol. 15, no. 12, 2023, Art. no. 3122.
- [237] E. Valencia et al., "Ocean surface's scattering coefficient retrieval by delay-Doppler map inversion," *IEEE Geosci. Remote Sens. Lett.*, vol. 8, no. 4, pp. 750–754, Jul. 2011.
- [238] E. Valencia, A. Camps, H. Park, N. Rodriguez-Alvarez, X. Bosch-Lluis, and I. Ramos-Pérez, "Oil slicks detection using GNSS-R," in *Proc. IEEE Int. Geosci. Remote Sens. Symp.*, 2011, pp. 4383–4386.
- [239] E. Valencia, A. Camps, N. Rodriguez-Alvarez, H. Park, and I. Ramos-Pérez, "Using GNSS-R imaging of the ocean surface for oil slick detection," *IEEE J. Sel. Topics Appl. Earth Observ. Remote Sens.*, vol. 6, no. 1, pp. 217–223, Feb. 2013.
- [240] W. Ji, C. Xiu, W. Li, and L. Wang, "Ocean surface target detection and positioning using the spaceborne GNSS-R delay-Doppler maps," in *Proc. IEEE Geosci. Remote Sens. Symp.*, 2014, pp. 3806–3809.
- [241] A. D. Simone, H. Park, D. Riccio, and A. Camps, "Sea target detection using spaceborne GNSS-R delay-Doppler maps: Theory and experimental proof of concept using TDS-1 data," *IEEE J. Sel. Topics Appl. Earth Observ. Remote Sens.*, vol. 10, no. 9, pp. 4237–4255, Sep. 2017.
- [242] J. W. Cheong, B. J. Southwell, and A. G. Dempster, "Blind sea clutter suppression for spaceborne GNSS-R target detection," *IEEE J. Sel. Topics Appl. Earth Observ. Remote Sens.*, vol. 12, no. 12, pp. 5373–5378, Dec. 2019.
- [243] B. J. Southwell, J. W. Cheong, and A. G. Dempster, "A matched filter for spaceborne GNSS-R based sea-target detection," *IEEE Trans. Geosci. Remote Sens.*, vol. 58, no. 8, pp. 5922–5931, Aug. 2020.
- [244] C. Liu et al., "Study on GNSS-R multi-target detection and location method based on consistency checking," *IET Radar, Sonar Navigation*, vol. 15, no. 6, pp. 605–617, 2021.
- [245] Y. Li, S. Yan, and J. Gong, "Target detection and location by fusing delay-Doppler maps," *IEEE Trans. Geosci. Remote Sens.*, vol. 61, 2023, Art. no. 5800114.
- [246] A. D. Simone, P. Braca, L. M. Millefiori, and P. Willett, "Ship detection using GNSS-reflectometry in backscattering configuration," in *Proc. IEEE Radar Conf.*, 2018, pp. 1589–1593.
- [247] A. Di Simone et al., "Spaceborne GNSS-reflectometry for ship-detection applications: Impact of acquisition geometry and polarization," in *Proc. IEEE Int. Geosci. Remote Sens. Symp.*, 2018, pp. 1071–1074.
- [248] A. di Simone et al., "Ship detection using GNSS-R delay-Doppler maps via simulation tools," in *Proc. IEEE 5th Int. Forum Res. Technol. Soc. Ind.*, 2019, pp. 109–114.
- [249] T. Beltramonte et al., "Simulation-based feasibility analysis of ship detection using GNSS-R delay-Doppler maps," *IEEE J. Sel. Topics Appl. Earth Observ. Remote Sens.*, vol. 13, pp. 1385–1399, 2020.
- [250] Z. Zhao, Z. Xia, Z. Xu, T. Zhang, and T. Peng, "A novel method of ship detection by combining space-borne SAR and GNSS-R," in *Proc. IET Int. Radar Conf.*, 2021, pp. 1045–1051.
- [251] M. C. Evans and C. S. Ruf, "Toward the detection and imaging of ocean microplastics with a spaceborne radar," *IEEE Trans. Geosci. Remote Sens.*, vol. 60, 2022, Art. no. 4202709.
- [252] A. Gonga, A. Pérez-Portero, A. Camps, D. Pascual, A. de Fockert, and P. de Maagt, "GNSS-R observations of marine plastic litter in a water flume: An experimental study," *Remote Sens.*, vol. 15, no. 3, 2023, Art. no. 637.
- [253] M. Hoseini, M. Asgarimehr, V. Zavorotny, H. Nahavandchi, C. Ruf, and J. Wickert, "First evidence of mesoscale ocean eddies signature in GNSS reflectometry measurements," *Remote Sens.*, vol. 12, no. 3, 2020, Art. no. 542.
- [254] M. Hoseini and H. Nahavandchi, "The potential of spaceborne GNSS reflectometry for detecting ocean surface currents," *Remote Sens. Environ.*, vol. 282, 2022, Art. no. 113256.
- [255] Y. Wang and Y. J. Morton, "Evaluation of GNSS-R retrieved sea ice surface height using ICESat-2 ice freeboard measurements," in *Proc. IEEE Int. Geosci. Remote Sens. Symp.*, 2021, pp. 7803–7806.
- [256] W. Li, E. Cardellach, F. Fabra, A. Rius, S. Ribo, and M. Martin-Neira, "First spaceborne phase altimetry over sea ice using TechDemoSat-1 GNSS-R signals," *Geophysical Res. Lett.*, vol. 44, no. 16, pp. 8369–8376, 2017.

- [257] R. N. Buendía, S. Tabibi, M. Talpe, and I. Otosaka, "Ice sheet height retrievals from Spire grazing angle GNSS-R," *Remote Sens. Environ.*, vol. 297, 2023, Art. no. 113757.
- [258] Y. Wang, "Grazing-angle GNSS-R for the determination of tropospheric delay and water vapor content," in *Proc. 36th Int. Tech. Meeting Satell. Division Inst. Navigation*, 2023, pp. 3227–3232.
- [259] Y. Wang, "Troposphere sensing using grazing-angle GNSS-R measurement from LEO satellites," *Geophysical Res. Lett.*, vol. 50, no. 24, 2023, Art. no. e2023GL106249.



Jinwei Bu (Member, IEEE) received the B.S. degree in surveying and mapping engineering and the M.S. degree in geodesy and surveying engineering from the Kunming University of Science and Technology, Kunming, China, in 2016 and 2018, respectively, and the Ph.D. degree in geodesy and surveying engineering from the School of Environmental Science and Spatial Informatics, China University of Mining and Technology, Xuzhou, China, in 2022.

He was a Visiting Ph.D. student with the Department of Signal Theory and Communications, Universitat Politècnica de Catalunya, Barcelona, Spain, from 2021 to 2022. He is currently a Master Supervisor with the Faculty of Land Resource Engineering, Kunming University of Science and Technology, Kunming. He has authored or coauthored more than 50 refereed journal articles. He serves as a reviewer for more than ten international journals, such as *IEEE TRANSACTIONS ON GEOSCIENCE AND REMOTE SENSING*, *GPS Solutions*, *IEEE Internet of Things Journal*, *Ocean Engineering*, *Remote Sensing, Measurement, Advances in Space Research*, and *Measurement Science and Technology*. His research interests include global navigation satellite systems (GNSS) reflectometry, GNSS atmospheric remote sensing, GNSS precision positioning, and machine/deep learning.



Xinyu Liu received the bachelor's degree in engineering from the City College of Kunming University of Science and Technology, Kunming, China, in July 2023. She is currently working toward the master's degree with the Faculty of Land Resource Engineering, Kunming University of Science and Technology, Kunming.

Her research interest is global navigation satellite systems reflectometry.



Jiulan Wang is currently working toward the B.S. degree in geographic information science with the Faculty of Land Resources Engineering, Kunming University of Science and Technology, Kunming, China.

Her research interest is global navigation satellite systems reflectometry.



Linghui Li received the bachelor's degree in surveying and mapping engineering from Nanyang Normal University, in 2021. She is currently working toward the master's degree in photogrammetry and remote sensing from Kunming University of Science and Technology in Kunming, China.

Her research interest is GNSS reflectometry.



Xiaoqing Zuo received the M.S. degree from the Kunming University of Science and Technology, Kunming, China, in 2001, and the Ph.D. degree from Wuhan University, Wuhan, China, in 2004, both in geographic information science.

He is currently a Professor with the Kunming University of Science and Technology. His main research interests include data mining, InSAR theory and technology, and remote sensing image processing and analysis.

Prof. Zuo was named Yunnan Young and Middle-Aged Academic and Technical Leaders Reserve Talent. He is also the Deputy Director of the GIS Professional Committee of the Yunnan Provincial Surveying and Mapping Society.



Kegen Yu (Senior Member, IEEE) received the Ph.D. degree in electrical engineering from The University of Sydney, Sydney, NSW, Australia, in 2003.

He was with Jiangxi Geological and Mineral Bureau, Nanchang, China; Nanchang University, Nanchang; the University of Oulu, Oulu, Finland; the CSIRO ICT Center, Sydney; Macquarie University, Sydney; the University of New South Wales, Sydney; and Wuhan University, Wuhan, China. He is currently a Professor with the School of Environment Science and Spatial Informatics, China University of Mining

and Technology, Xuzhou, China. He has coauthored the book *Ground-Based Wireless Positioning* (Wiley and IEEE Press, 2009), a Chinese version of the book is also available, and another book *Wireless Positioning: Principles and Practice* (Springer, 2018). He has authored the book *Theory and Practice of GNSS Reflectometry* (Springer, 2021). He edited the book *Positioning and Navigation in Complex Environments* (IGI Global, 2018) and the book *Indoor Positioning and Navigation* (Science Press, 2019). He has authored or coauthored more than 150 refereed journal articles and 60 conference papers. He is on the list of world's top 2% most-cited scientists in 2022 by Stanford University. His research interests include global navigation satellite systems reflectometry, ground- and satellite-based positioning, and remote sensing.



Weimin Huang (Senior Member, IEEE) received the B.S., M.S., and Ph.D. degrees in radio physics from Wuhan University, Wuhan, China, in 1995, 1997, and 2001, respectively, and the M.Eng. degree in electrical engineering from the Memorial University of Newfoundland, St. John's, NL, Canada, in 2004.

From 2008 to 2010, he was a Design Engineer with Rutter Technologies, St. John's. Since 2010, he has been with the Faculty of Engineering and Applied Science, Memorial University of Newfoundland, where

he is currently a Professor. He has authored or coauthored more than 290 refereed research articles. He has edited the book *Ocean Remote Sensing Technologies: High Frequency, Marine, and GNSS-Based Radar*. His research interests include mapping of oceanic surface parameters via high-frequency ground wave radar, X-band marine radar, synthetic aperture radar, and global navigation satellite systems.

Dr. Huang was a Member and the Co-Chair of the Electrical and Computer Engineering Evaluation Group for Natural Sciences and Engineering Research Council of Canada Discovery Grants from 2018 to 2021. He has been a Technical Program Committee Member. He was a recipient of a Postdoctoral Fellowship from the Memorial University of Newfoundland, the Discovery Accelerator Supplements Award from NSERC in 2017, and IEEE Geoscience and Remote Sensing Society 2019 Letters Prize Paper Award, as well as some other teaching and research awards. He is also an Area Editor for *IEEE Canadian Journal of Electrical and Computer Engineering*, an Associate Editor for *IEEE TRANSACTIONS ON GEOSCIENCE AND REMOTE SENSING*, *IEEE Geoscience and Remote Sensing Letters*, *IEEE Journal of Oceanic Engineering*, *Remote Sensing, Frontiers in Marine Science*, and is the Guest Editor for *IEEE Journal of Selected Topics In Applied Earth Observations and Remote Sensing* and five other journals. He is a reviewer for more than 120 international journals and a reviewer for many IEEE international conferences, such as RadarCon, International Conference on Communications, IEEE Global Communications Conference, and IEEE International Geoscience and Remote Sensing Symposium, and Oceans. He was the General Co-Chair and the Technical Program Co-Chair for the IEEE Oceanic Engineering Society 13th Currents, Waves, and Turbulence Measurement Workshop.